Scattering computations using a rotationally symmetric solver implemented in open source finite elements

Sjöberg, Daniel

2025

CODEN:LUTEDX/(TEAT-7284)/1-32/(2025)

Scattering computations using a rotationally symmetric solver implemented in open source finite elements

Daniel Sjöberg

Electromagnetic Theory
Department of Electrical and Information Technology
Lund University
Sweden

(TEAT-7284)/1-32/(2025): D. Sjöberg, Computation of Radome Reference Cases

Daniel Sjöberg
daniel.sjoberg@eit.lth.se

Department of Electrical and Information Technology
Electromagnetic Theory
Lund University
P.O. Box 118
SE-221 00 Lund
Sweden

Editor: Mats Gustafsson

Abstract

We summarize the theory and implementation of an open source solver for rotationally symmetric scatterers. The purpose of the code is to compute reference solutions for electrically large radome problems. The rotational symmetry decouples the azimuthal modes, enabling the three-dimensional problem to be broken down into a sequence of decoupled two-dimensional problems which require much less memory than the original problem. The code is based on the open source finite elements code FEniCSx, which also supports parallelization using MPI, allowing further scaling of the problem size. The developed code can handle excitation as incident plane waves or a transmitting antenna, and can output near field data for visualization as well as far field data in cuts or projected on spherical vector wave expansions for further post processing. The performance is verified for Mie scattering agains metal and dielectric spheres, and a realistic radome geometry is simulated and discussed.

1 Introduction

For several applications, there is a need for accurate solutions of electrically large problems, that is, where the geometry is large in terms of wavelengths. A particular case is in the design and analysis of radomes, which are structures enclosing antennas in order to protect them from wear and tear [6, 14]. The antenna is often a large array antenna with hundreds or thousands of elements, making the radome necessarily in the order of tens or hundreds of wavelengths [10]. When designing these radomes, various approximations are usually necessary in the simulations and it is of interest to develop reference cases where the approximate methods can be benchmarked.

Previous efforts in this direction based on spherically symmetric structures were presented in [7, 8], and for rotationally symmetric structures with a highly symmetric excitation in [15]. In this paper, we generalize the results in [15] to enable arbitrary excitations. The methodology is based on the fact that for rotationally symmetric geometries, Maxwell's equations decouple into a sequence of two-dimensional problems for each azimuthal mode, where each problem is much smaller than the original three-dimensional problem. This makes it feasible to simulate large geometries with limited memory resources, and enables the development of realistic reference problems for approximate methods. In this paper, we study an ogive-shaped radome containing a circular antenna with an amplitude tapering that provides low side lobe levels. The interaction of the antenna boundary with the radome structure has been studied in more detail in [16].

2 Rotational symmetry

The simulation of a three-dimensional geometry that has rotational symmetry can be broken down into a sequence of two-dimensional cross-sectional problems. This represents a huge saving in computational complexity, making it possible to simulate very large problems using moderate hardware in terms of memory, although the total

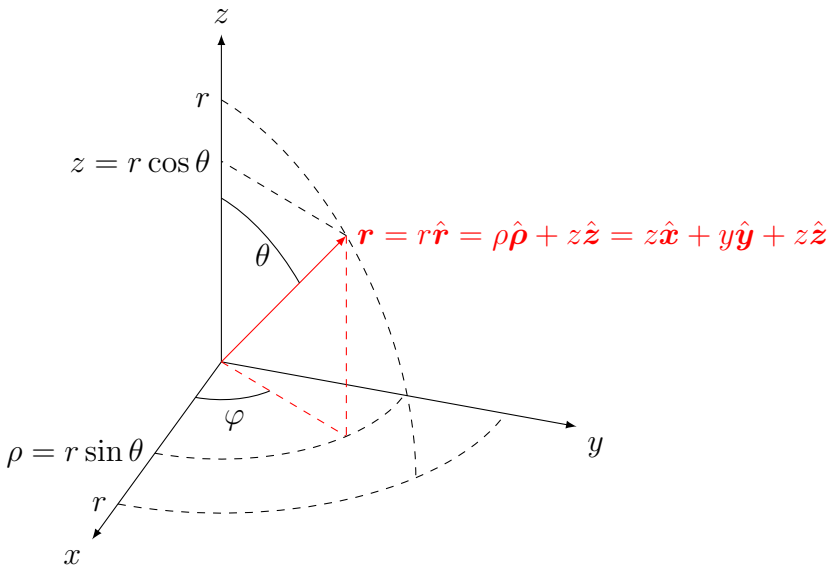

Figure 1: Cartesian, cylindrical, and spherical coordinate systems.

amount of azimuthal modes to be simulated may still be significant. The number of modes necessary is determined from the Wiscombe criterion for Mie scattering [18], which in its most restrictive form is

$$N > ka + 4.05(ka)^3 + 2, \tag{2.1}$$

where a is the radius of the scattering region, and $k = 2\pi/\lambda$ is the free space wavenumber, λ being the free space wavelength. The azimuthal modes are indexed by m with $-N \leq m \leq N$. The number N can be significantly reduced if the excitation also has high symmetry, for instance for waves propagating along the symmetry axis [15].

2.1 Representation in cylindrical coordinates

To demonstrate how a rotationally symmetric problem can be decomposed into a sequence of cross-sectional problems, we consider the representation of a time-harmonic (time convention $\mathrm{e}^{\mathrm{j}\omega t}$ where ω is the angular frequency) electromagnetic field in cylindrical coordinates (ρ, φ, z), see Figure 1. The result is

$$\boldsymbol{E}(\boldsymbol{r}) = \sum_{m=-\infty}^{\infty} \boldsymbol{E}^{(m)}(\rho, z)\mathrm{e}^{-\mathrm{j}m\varphi} = \sum_{m=-\infty}^{\infty} \left[E_\rho^{(m)}(\rho, z)\hat{\boldsymbol{\rho}} + E_\varphi^{(m)}(\rho, z)\hat{\boldsymbol{\varphi}} + E_z^{(m)}(\rho, z)\hat{\boldsymbol{z}}\right] \mathrm{e}^{-\mathrm{j}m\varphi}, \tag{2.2}$$

$$\boldsymbol{H}(\boldsymbol{r}) = \sum_{m=-\infty}^{\infty} \boldsymbol{H}^{(m)}(\rho, z)\mathrm{e}^{-\mathrm{j}m\varphi} = \sum_{m=-\infty}^{\infty} \left[H_\rho^{(m)}(\rho, z)\hat{\boldsymbol{\rho}} + H_\varphi^{(m)}(\rho, z)\hat{\boldsymbol{\varphi}} + H_z^{(m)}(\rho, z)\hat{\boldsymbol{z}}\right] \mathrm{e}^{-\mathrm{j}m\varphi}, \tag{2.3}$$

where the importance is that the azimuth angular dependence $\mathrm{e}^{-\mathrm{j}m\varphi}$ has been factored out from each term in the series. By defining the differential operator ∇_m as

$$\begin{aligned}\nabla_m \times \boldsymbol{E}^{(m)} &= \mathrm{e}^{\mathrm{j}m\varphi}\nabla \times (\boldsymbol{E}^{(m)}\mathrm{e}^{-\mathrm{j}m\varphi}) \\ &= \hat{\boldsymbol{\rho}}\left(-\frac{\mathrm{j}m}{\rho}E_z^{(m)} - \frac{\partial E_\varphi^{(m)}}{\partial z}\right) + \hat{\boldsymbol{\varphi}}\left(\frac{\partial E_\rho^{(m)}}{\partial z} - \frac{\partial E_z^{(m)}}{\partial \rho}\right) + \hat{\boldsymbol{z}}\left(\frac{1}{\rho}\frac{\partial}{\partial \rho}(\rho E_\varphi^{(m)}) + \frac{\mathrm{j}m}{\rho}E_\rho^{(m)}\right),\end{aligned} \tag{2.4}$$

it is clear that after multiplying with $\mathrm{e}^{\mathrm{j}m\varphi}$ and integrating over φ (assuming ϵ and μ are independent of φ), Maxwell's equations become

$$\begin{cases} \displaystyle\int_0^{2\pi} \mathrm{e}^{\mathrm{j}m\varphi}(\nabla \times \boldsymbol{E} + \mathrm{j}\omega\mu\boldsymbol{H})\,\mathrm{d}\varphi = \boldsymbol{0} \\ \displaystyle\int_0^{2\pi} \mathrm{e}^{\mathrm{j}m\varphi}(\nabla \times \boldsymbol{H} - \mathrm{j}\omega\epsilon\boldsymbol{E})\,\mathrm{d}\varphi = \boldsymbol{0} \end{cases} \quad \Rightarrow \quad \begin{cases} \nabla_m \times \boldsymbol{E}^{(m)} + \mathrm{j}\omega\mu\boldsymbol{H}^{(m)} = \boldsymbol{0} \\ \nabla_m \times \boldsymbol{H}^{(m)} - \mathrm{j}\omega\epsilon\boldsymbol{E}^{(m)} = \boldsymbol{0} \end{cases} \tag{2.5}$$

where ∇_m differentiates in ρ and z only. Hence, we have a two-dimensional cross-sectional problem to solve for the modal amplitudes $\boldsymbol{E}^{(m)}(\rho, z)$ and $\boldsymbol{H}^{(m)}(\rho, z)$. In a finite element context, it is customary to use Faraday's law to eliminate the magnetic field, providing the second order partial differential equation in two spatial dimensions (ρ, z)

$$-\nabla_m \times (\mu_\mathrm{r}^{-1}\nabla_m \times \boldsymbol{E}^{(m)}) + k^2\epsilon_\mathrm{r}\boldsymbol{E}^{(m)} = \boldsymbol{0} \tag{2.6}$$

for the electric field $\boldsymbol{E}^{(m)}$, where we introduced the relative permeability $\mu_\mathrm{r} = \mu/\mu_0$, relative permittivity $\epsilon_\mathrm{r} = \epsilon/\epsilon_0$, and the vacuum wavenumber $k = \omega\sqrt{\epsilon_0\mu_0} = 2\pi/\lambda$.

The weak formulation of (2.6) is found by multiplying with a test function $\boldsymbol{v}$ and integrating over the domain. By also performing a partial integration, one of the curl operations is transferred to the test function and we have

$$\iint \left\{-\mu_\mathrm{r}^{-1}(\nabla_m \times \boldsymbol{E}^{(m)}) \cdot (\nabla_m \times \boldsymbol{v}) + k^2\epsilon_\mathrm{r}\boldsymbol{E}^{(m)} \cdot \boldsymbol{v}\right\} \rho\,\mathrm{d}\rho\,\mathrm{d}z = 0, \tag{2.7}$$

where we have neglected any boundary conditions in order to illustrate the basic structure of the expression. Note the multiplication with ρ at the end, which comes from the differential volume element in cylindrical coordinates, $\mathrm{d}V = \rho\,\mathrm{d}\rho\,\mathrm{d}z\,\mathrm{d}\varphi$.

2.2 Finite element formulation

The finite element method (FEM) formulation of the problem is based on the weak formulation (2.7). The sought field is expanded in basis functions as $\boldsymbol{E}^{(m)}(\boldsymbol{r}) = \sum_n E_n^{(m)}\boldsymbol{E}_n(\boldsymbol{r})$, and for each test function $\boldsymbol{v}(\boldsymbol{r})$, the equation (2.7) represents a row of a linear system of equations $Ax = b$ with x as the vector of unknowns $\{E_1^{(m)}, E_2^{(m)}, \ldots\}$ which can be solved for. The process can be significantly automated with the use of, for instance, the open source FEM project FEniCSx [2, 3, 12, 13],

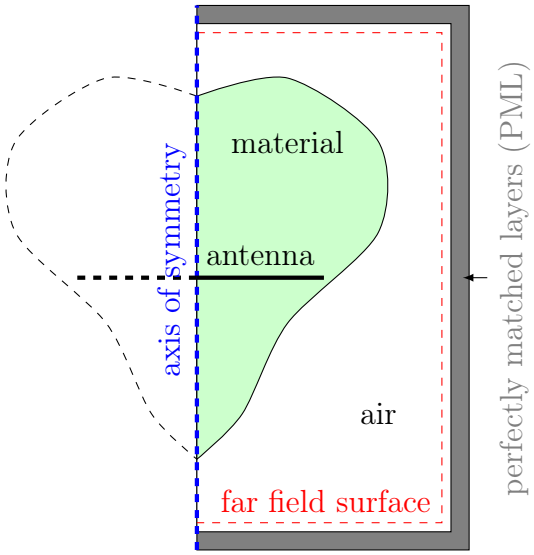

Figure 2: Geometry of the finite element simulation. The material region has material parameters different than air, and the air region has $\epsilon_{\mathrm{r}} = \mu_{\mathrm{r}} = 1$. The antenna consists of a closed surface where one part is an aperture with a prescribed antenna field $\boldsymbol{E}_{\mathrm{a}}$, and the other parts are PEC. The field on the far field surface is saved and postprocessed for each simulation. The simulation region (air and scatterer) Ω is surrounded by a region Ω_{pml} of perfectly matched layers, having relative permittivity tensor $\boldsymbol{\epsilon}_{\mathrm{r,pml}}$ and relative permeability tensor $\boldsymbol{\mu}_{\mathrm{r,pml}}$.

where all necessary basis functions and infrastructure for mesh handling, computing integrals and much more is already implemented. In this paper, the finite element is chosen as a mixed element, representing (E_ρ, E_z) with curl conforming first kind Nédélec (N1curl), and E_φ with node based Lagrange (CG) elements. The polynomial degree of the finite element can be chosen as a parameter in FEniCSx.

In order to truncate (2.6) to a finite domain Ω, we surround the domain of interest with an absorbing perfectly matched layer (PML) with complex and anisotropic material parameters $\boldsymbol{\epsilon}_{\mathrm{r,pml}}$ and $\boldsymbol{\mu}_{\mathrm{r,pml}}$ based on stretched coordinates, see Figure 2 and Appendix A for explicit expressions of the material parameters.

We include two different excitations: an antenna field $\boldsymbol{E}_\mathrm{a}$ which is present only as tangential components on the aperture Γ_ant of an antenna, and a background field $\boldsymbol{E}_\mathrm{b}$ which corresponds to an incident wave propagating in a background medium characterized by $\epsilon_\mathrm{r,b}$ and $\mu_\mathrm{r,b}$. Typically, the background medium is considered to be free space and we have $\epsilon_\mathrm{r,b} = \mu_\mathrm{r,b} = 1$. We need to enforce boundary conditions on the antenna surfaces, consisting of both perfect electric conductor (PEC) parts, and an antenna aperture. On the PEC surfaces Γ_pec, we require the boundary condition $\hat{\boldsymbol{n}} \times (\boldsymbol{E}^{(m)} + \boldsymbol{E}_\mathrm{b}^{(m)}) = \boldsymbol{0}$, where $\hat{\boldsymbol{n}}$ is the surface normal and $\boldsymbol{E}^{(m)} + \boldsymbol{E}_\mathrm{b}^{(m)}$ represents the total electric field. This is usually implemented as Dirichlet boundary conditions, where the degrees of freedom corresponding to the tangential electric fields are prescribed. However, it can also be straight-forwardly implemented in weak form by Nitsche's method [9]. This uses the functional

$$\frac{\alpha}{h} \int_{\Gamma_\mathrm{pec}} [\hat{\boldsymbol{n}} \times (\boldsymbol{E}^{(m)} + \boldsymbol{E}_\mathrm{b}^{(m)})] \cdot [\hat{\boldsymbol{n}} \times \boldsymbol{v}] \rho \, \mathrm{d}\ell, \tag{2.8}$$

where h is the triangle diameter and α is a tuning parameter, chosen as $\alpha = 10$ in this work. On the antenna aperture Γ_ant, we require the boundary condition $\hat{\boldsymbol{n}} \times (\boldsymbol{E}^{(m)} + \boldsymbol{E}_\mathrm{b}^{(m)} - \boldsymbol{E}_\mathrm{a}^{(m)}) = \boldsymbol{0}$, which can be implemented by the functional

$$\frac{\alpha}{h} \int_{\Gamma_\mathrm{ant}} [\hat{\boldsymbol{n}} \times (\boldsymbol{E}^{(m)} + \boldsymbol{E}_\mathrm{b}^{(m)} - \boldsymbol{E}_\mathrm{a}^{(m)})] \cdot [\hat{\boldsymbol{n}} \times \boldsymbol{v}] \rho \, \mathrm{d}\ell. \tag{2.9}$$

This treats the antenna aperture surface as a metal boundary with reflection coefficient -1 for the background field. The excitation $\boldsymbol{E}_\mathrm{a}$ for an antenna transmitting in a certain direction can be approximated as the field values of a plane wave propagating in the same direction evaluated on the antenna surface Γ_ant, see Appendix B. In total, our finite element formulation of the problem is then

$$\begin{aligned}
&\iint_\Omega \left\{ -\mu_\mathrm{r}^{-1} [\nabla_m \times \boldsymbol{E}^{(m)}] \cdot (\nabla_m \times \boldsymbol{v}) + k^2 \epsilon_\mathrm{r} \boldsymbol{E}^{(m)} \cdot \boldsymbol{v} \right\} \rho \, \mathrm{d}\rho \, \mathrm{d}z \\
&\quad + \iint_{\Omega_\mathrm{pml}} \left\{ -[\boldsymbol{\mu}_\mathrm{r,pml}^{-1} \cdot (\nabla_m \times \boldsymbol{E}^{(m)})] \cdot (\nabla_m \times \boldsymbol{v}) + k^2 [\boldsymbol{\epsilon}_\mathrm{r,pml} \cdot \boldsymbol{E}^{(m)}] \cdot \boldsymbol{v} \right\} \rho \, \mathrm{d}\rho \, \mathrm{d}z \\
&+ \frac{\alpha}{h} \int_{\Gamma_\mathrm{pec}} [\hat{\boldsymbol{n}} \times (\boldsymbol{E}^{(m)} + \boldsymbol{E}_\mathrm{b}^{(m)})] \cdot [\hat{\boldsymbol{n}} \times \boldsymbol{v}] \rho \, \mathrm{d}\ell + \frac{\alpha}{h} \int_{\Gamma_\mathrm{ant}} [\hat{\boldsymbol{n}} \times (\boldsymbol{E}^{(m)} + \boldsymbol{E}_\mathrm{b}^{(m)} - \boldsymbol{E}_\mathrm{a}^{(m)})] \cdot [\hat{\boldsymbol{n}} \times \boldsymbol{v}] \rho \, \mathrm{d}\ell \\
&\quad + \iint_\Omega k^2 (\epsilon_\mathrm{r} - \mu_\mathrm{r}^{-1} \mu_\mathrm{r,b} \epsilon_\mathrm{r,b}) \boldsymbol{E}_\mathrm{b}^{(m)} \cdot \boldsymbol{v} \rho \, \mathrm{d}\rho \, \mathrm{d}z = 0.
\end{aligned} \tag{2.10}$$

The last row is what remains after considering Maxwells' equations for the total field $\boldsymbol{E}^{(m)} + \boldsymbol{E}_{\mathrm{b}}^{(m)}$, and using that the background field $\boldsymbol{E}_{\mathrm{b}}^{(m)}$ satisfies the equation $\iint_\Omega \mu_{\mathrm{r,b}}^{-1}(\nabla_m \times \boldsymbol{E}_{\mathrm{b}}^{(m)}) \cdot (\nabla_m \times \boldsymbol{v})\rho \,\mathrm{d}\rho \,\mathrm{d}z = \iint_\Omega \epsilon_{\mathrm{r,b}} k^2 \boldsymbol{E}_{\mathrm{b}}^{(m)} \cdot \boldsymbol{v}\rho \,\mathrm{d}\rho \,\mathrm{d}z$. Usually, only one of the excitations $\boldsymbol{E}_{\mathrm{a}}$ or $\boldsymbol{E}_{\mathrm{b}}$ is nonzero.

2.3 Symmetries

Considering each polarization of an incident plane wave or antenna excitation according to Appendix B and the general relation $\mathrm{J}_{-n}(x) = (-1)^n \mathrm{J}_n(x)$, it is clear the solution has the parities

θ-polarization	ϕ-polarization	
$E_\rho^{(-m)} = +E_\rho^{(m)}$	$E_\rho^{(-m)} = -E_\rho^{(m)}$	(2.11)
$E_z^{(-m)} = +E_z^{(m)}$	$E_z^{(-m)} = -E_z^{(m)}$	(2.12)
$E_\varphi^{(-m)} = -E_\varphi^{(m)}$	$E_\varphi^{(-m)} = +E_\varphi^{(m)}$	(2.13)

Hence, for a fixed polarization it is sufficient to compute the solution for $m \geq 0$, and synthesize the solution in postprocess. When polarizations are mixed, for instance one polarization of an incident wave and another for the antenna excitation, no symmetries can be used.

3 Implementation in FEniCSx

The formulation (2.10) has been implemented in FEniCSx, and is available at `https://github.com/dsjoberg-git/rotsymsca`. The implementation is largely inspired by the dolfinx demo *Electromagnetic scattering from a sphere (asisymmetric)* at `https://docs.fenicsproject.org/dolfinx/v0.9.0/python/demos/demo_axis.html`. The key steps of the code are

- Create a mesh for the geometry using the Python interface to the open source mesh program Gmsh (`https://gmsh.info/`) [4]. At this stage, it is important to correctly label the geometry to identify regions with different materials and boundary conditions and pass this on to the main FEniCSx code.
- Represent the three-dimensional electric field with a mixed finite element, where the in-plane field components (E_ρ, E_z) are represented with Nédélec curl-conforming elements, and the out-of-plane field E_ϕ is represented with scalar node-based Lagrange elements. The polynomial degree of the finite elements can be chosen freely.
- Set up material parameters and boundary conditions of the problem. This includes computing the PML material parameters using the expressions in Appendix A.
- Compute the solutions for each azimuth mode index m, and save relevant data for postprocessing.

- Perform relevant postprocessing such as far field computation, near field plots, and projection on spherical vector harmonics.

Parallel processing using message passing interface (MPI) is mostly transparent in FEniCSx, but requires attention in the postprocess stage, where results from the different processes need to be gathered in one single process. As of fall 2024, it is not possible to save the solution when running in parallel (this is under current development in FEniCSx), so only processed data is saved.

The code is provided as a main library `rotsymsca.py`, which can be loaded in simulation scripts, see `verification.py` and `radome_simulations.py` for examples. The mesh is generated in `mesh_rotsymradome.py`.

4 Post processing

Since the field is computed for each azimuthal mode, some non-trivial post processing is necessary to obtain the desired output data. This data is primarily the far field amplitude, which can either be computed directly or by first projecting the solution on the spherical vector harmonics. For visualization purposes, we also need to consider near field data.

4.1 Far field computations

If the tangential electric and magnetic fields on a general surface S with outward normal $\hat{\boldsymbol{n}}$ have been computed, the far field amplitude in direction $\hat{\boldsymbol{k}}$ is given by

$$\boldsymbol{F}(\hat{\boldsymbol{k}}) = \frac{\mathrm{j}k}{4\pi}\hat{\boldsymbol{k}} \times \iint_S \Big[\boldsymbol{E}(\boldsymbol{r}) \times \hat{\boldsymbol{n}} + \eta_0 \hat{\boldsymbol{k}} \times (\hat{\boldsymbol{n}} \times \boldsymbol{H}(\boldsymbol{r}))\Big] \, \mathrm{e}^{\mathrm{j}k\hat{\boldsymbol{k}}\cdot\boldsymbol{r}} \, \mathrm{d}S. \tag{4.1}$$

In the specific case of a rotationally symmetric structure, the surface S is described by a curve γ in the ρ-z plane, and we have $\boldsymbol{F}(\hat{\boldsymbol{k}}) = \sum_m \boldsymbol{F}^{(m)}(\hat{\boldsymbol{k}})$ where

$$\boldsymbol{F}^{(m)}(\hat{\boldsymbol{k}}) = \frac{\mathrm{j}k}{4\pi}\hat{\boldsymbol{k}} \times \int_{\boldsymbol{\rho}\in\gamma} \int_{\varphi=0}^{2\pi} \Big[\boldsymbol{E}^{(m)}(\rho, z) \times \hat{\boldsymbol{n}} + \eta_0 \hat{\boldsymbol{k}} \times (\hat{\boldsymbol{n}} \times \boldsymbol{H}^{(m)}(\rho, z))\Big] \, \mathrm{e}^{\mathrm{j}(k\hat{\boldsymbol{k}}\cdot\boldsymbol{r} - m\varphi)} \rho \, \mathrm{d}\varphi \, \mathrm{d}\ell \tag{4.2}$$

The integral in the φ-direction is explicitly computed in Appendix C, using the parameterization $\hat{\boldsymbol{k}} = \hat{\boldsymbol{x}} \sin\theta\cos\phi + \hat{\boldsymbol{y}} \sin\theta \sin\phi + \hat{\boldsymbol{z}} \cos\theta$, where θ is the polar angle and ϕ the azimuth angle. Note that we distinguish between the far field direction azimuth angle ϕ and the azimuth angle φ used in the cylindrical coordinate system

where the vector components of the electric field are defined. The result is

$$\begin{aligned}
\boldsymbol{F}^{(m)}(\theta,\phi) = \hat{\boldsymbol{\theta}}\frac{\mathrm{j}k}{2}\mathrm{j}^m\mathrm{e}^{-\mathrm{j}m\phi}\int_{\boldsymbol{\rho}\in\gamma}\Big\{ &-\left[C_m n_z E_\varphi^{(m)} - S_m(n_\rho E_z^{(m)} - n_z E_\rho^{(m)})\right]\sin\phi \\
&+\left[S_m n_z E_\varphi^{(m)} + C_m(n_\rho E_z^{(m)} - n_z E_\rho^{(m)})\right]\cos\phi \\
&-\eta_0\left[C_m n_z H_\varphi^{(m)} - S_m(n_\rho H_z^{(m)} - n_z H_\rho^{(m)})\right]\cos\theta\cos\phi \\
&-\eta_0\left[S_m n_z H_\varphi^{(m)} + C_m(n_\rho H_z^{(m)} - n_z H_\rho^{(m)})\right]\cos\theta\sin\phi \\
&+\eta_0 A_m n_\rho H_\varphi^{(m)}\sin\theta\Big\}\mathrm{e}^{\mathrm{j}kz\cos\theta}\rho\,\mathrm{d}\ell \\
+\hat{\boldsymbol{\phi}}\frac{\mathrm{j}k}{2}\mathrm{j}^m\mathrm{e}^{-\mathrm{j}m\phi}\int_{\boldsymbol{\rho}\in\gamma}\Big\{ &-\left[C_m n_z E_\varphi^{(m)} - S_m(n_\rho E_z^{(m)} - n_z E_\rho^{(m)})\right]\cos\theta\cos\phi \\
&-\left[S_m n_z E_\varphi^{(m)} + C_m(n_\rho E_z^{(m)} - n_z E_\rho^{(m)})\right]\cos\theta\sin\phi \\
&+A_m n_\rho E_\varphi^{(m)}\sin\theta \\
&+\eta_0\left[C_m n_z H_\varphi^{(m)} - S_m(n_\rho H_z^{(m)} - n_z H_\rho^{(m)})\right]\sin\phi \\
&-\eta_0\left[S_m n_z H_\varphi^{(m)} + C_m(n_\rho H_z^{(m)} - n_z H_\rho^{(m)})\right]\cos\phi\Big\}\mathrm{e}^{\mathrm{j}kz\cos\theta}\rho\,\mathrm{d}\ell
\end{aligned} \tag{4.3}$$

where

$$A_m = \mathrm{J}_m(k\rho\sin\theta) \tag{4.4}$$

$$C_m = \frac{1}{2}\left[\mathrm{e}^{\mathrm{j}\phi}\,\mathrm{J}_{m-1}(k\rho\sin\theta) + \mathrm{e}^{-\mathrm{j}\phi}\,\mathrm{J}_{m+1}(k\rho\sin\theta)\right] \tag{4.5}$$

$$S_m = \frac{\mathrm{j}}{2}\left[\mathrm{e}^{\mathrm{j}\phi}\,\mathrm{J}_{m-1}(k\rho\sin\theta) - \mathrm{e}^{-\mathrm{j}\phi}\,\mathrm{J}_{m+1}(k\rho\sin\theta)\right] \tag{4.6}$$

This integral has been implemented in FEniCSx. It is important to restrict the evaluations of the Bessel functions to cells adjacent to the farfield boundary, in order to keep the overhead computations to a minimum.

4.2 Projection on spherical vector harmonics

In order to limit the data needed to be saved from each simulation, the far field results can be projected on spherical vector harmonics, which also enables post-processing of a three-dimensional radiation pattern. We follow the definitions of spherical vector harmonics presented in [5], which is based on time convention $\mathrm{e}^{-\mathrm{i}\omega t}$, whereas this document uses time convention $\mathrm{e}^{\mathrm{j}\omega t}$. Define

$$(\boldsymbol{E}_{smn}^{(c)}, \boldsymbol{H}_{smn}^{(c)}) = \left(k\sqrt{\eta}\boldsymbol{F}_{smn}^{(c)}(r,\theta,\varphi), \frac{-\mathrm{i}k}{\sqrt{\eta}}\boldsymbol{F}_{3-s,m,n}^{(c)}(r,\theta,\varphi)\right) \tag{4.7}$$

where $\boldsymbol{F}_{smn}^{(c)}(r,\theta,\varphi)$ denotes the spherical vector waves as defined in [5], and $\eta = \sqrt{\mu_0/\epsilon_0}$ is the wave impedance (note that [5] uses the letter η for the wave admittance, that is, $\eta_{\text{Hansen}} = \sqrt{\epsilon_0/\mu_0}$). The outgoing field is given by $c = 3$ as

$$(\boldsymbol{E}(\boldsymbol{r}), \boldsymbol{H}(\boldsymbol{r})) = \sum_{smn} Q_{smn}^{(3)}(\boldsymbol{E}_{smn}^{(3)}(\boldsymbol{r}), \boldsymbol{H}_{smn}^{(3)}(\boldsymbol{r})), \tag{4.8}$$

where the expansion coefficients $Q^{(3)}_{smn}$ are determined from the integral (where $\boldsymbol{E}$ and $\boldsymbol{H}$ are the electric and magnetic field from the simulation, respectively)

$$\iint_S \left\{ \boldsymbol{E} \times \boldsymbol{H}^{(1)}_{s,-m,n} - \boldsymbol{E}^{(1)}_{s,-m,n} \times \boldsymbol{H} \right\} \cdot \hat{\boldsymbol{n}} \, \mathrm{d}S = (-1)^{m+1} Q^{(3)}_{smn}. \tag{4.9}$$

The far field amplitude is

$$\begin{aligned} \boldsymbol{F}(\theta,\varphi) = \lim_{r\to\infty} \frac{r}{\mathrm{e}^{\mathrm{i}kr}} \sum_{smn} Q^{(3)}_{smn} \boldsymbol{E}^{(3)}_{smn}(r,\theta,\varphi) &= \lim_{r\to\infty} \frac{kr}{\mathrm{e}^{\mathrm{i}kr}} \sqrt{4\pi} \sqrt{\frac{\eta}{4\pi}} \sum_{smn} Q^{(3)}_{smn} \boldsymbol{F}^{(3)}_{smn}(r,\theta,\varphi) \\ &= \sqrt{\frac{\eta}{4\pi}} \sum_{smn} Q^{(3)}_{smn} \boldsymbol{K}_{smn}(\theta,\varphi), \end{aligned} \tag{4.10}$$

where the functions $\boldsymbol{K}_{smn}(\theta,\varphi)$ are given in [5]. In order to use this procedure together with our fields that have been computed using time convention $\mathrm{e}^{\mathrm{j}\omega t}$, we first take the complex conjugate of our fields $(\boldsymbol{E}, \boldsymbol{H})$ that are recorded on a far field boundary. We then compute the expansion coefficients $Q^{(3)}_{smn}$, and compute the far field amplitude using (4.10), and finally take the complex conjugate of this result to obtain the expansion coefficients relevant for the time convention $\mathrm{e}^{\mathrm{j}\omega t}$.

When only a cut of the far field amplitude is necessary, it is usually faster to just compute the far field directly using the method in Section 4.1. But when the far field should be evaluated on the whole sphere, there is a clear benefit in first computing the expansion coefficients $Q^{(3)}_{smn}$ which can subsequently be used for any postprocessing of the far field.

4.3 Near field plots

For visualization purposes, it is necessary to compute the complex amplitude of the near fields. We then need to compute the following sum

$$\boldsymbol{E}(\boldsymbol{r}) = \sum_{m=-N}^{N} \boldsymbol{E}^{(m)}(\boldsymbol{r}) \mathrm{e}^{-\mathrm{j}m\varphi} \tag{4.11}$$

for a fixed azimuth angle φ (typically $\varphi = 0$). Since each azimuth mode is computed sequentially, we create a stored field $\boldsymbol{E}(\boldsymbol{r})$ and add each mode sequentially according to (4.11) until all modes have been computed. In order to plot a full cross section, this means we need to compute the near field not only for $\varphi = 0$, but also for $\varphi = \pi$. Animations of the near field can be created by plotting a sequence of $\mathrm{Re}\{\boldsymbol{E}(\boldsymbol{r})\mathrm{e}^{\mathrm{j}\omega t}\}$ for $\omega t \in [0, 2\pi]$.

5 Verification

The code has been verified by computing the differential scattering cross section for two spheres, one having radius $\lambda/2$ and the other having radius 3λ. We consider both

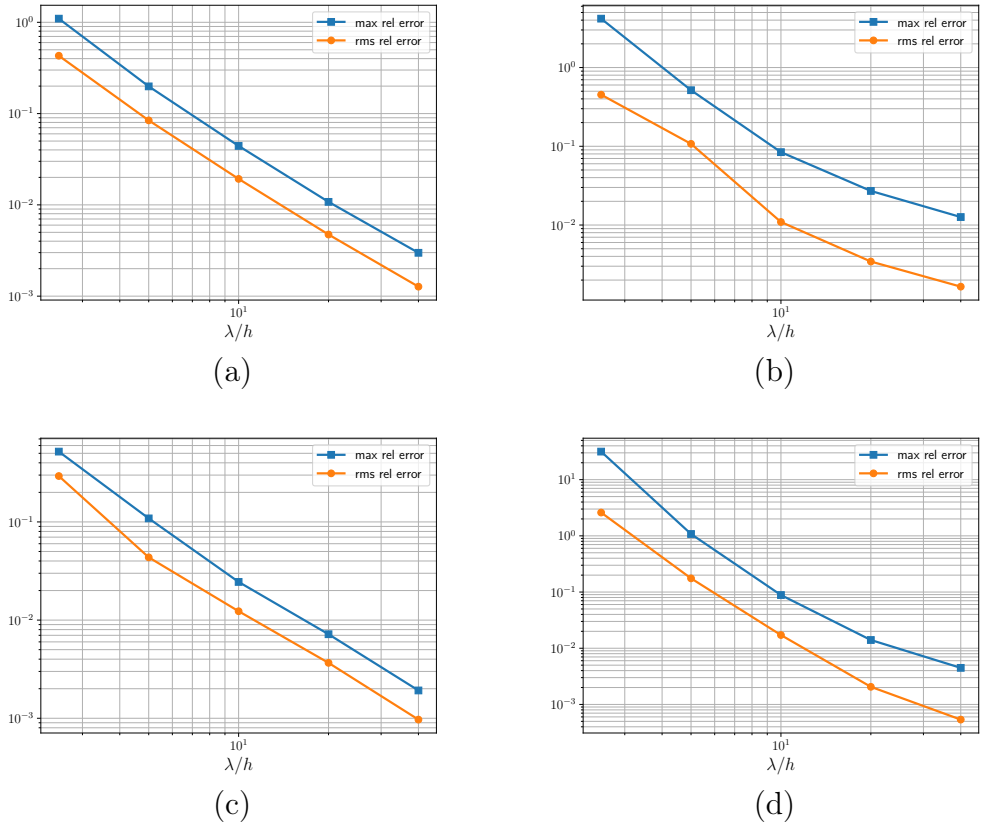

Figure 3: Results for h-convergence of E-plane differential scattering cross section of some spheres. (a) PEC sphere radius $\lambda/2$, (b) PEC sphere radius 3λ, (c) lossy dielectric sphere radius $\lambda/2$, (d) lossy dielectric sphere radius 3λ.

PEC spheres and lossy dielectric spheres, having relative permittivity $3(1 - 0.1\mathrm{j})$. The degree of the finite elements is kept constant at 3, and the mesh size is varied as $h/\lambda \in [0.4, 0.2, 0.1, 0.05, 0.025]$. The farfield surface is at $\lambda/2$ from the sphere surface, the PML starts at $\lambda/2$ from the farfield surface, and is $\lambda/2$ thick. The differential scattering cross section is computed for a wave incident at $\theta = 0$ and $\phi = 0$, where it is sufficient to use only modes $m = \pm 1$ to represent the plane wave. The error is computed using the results from miepython [11] as reference value. The results for E-plane scattering are shown in Figure 3, and the H-plane results are in Figure 4.

It is seen that there is a clear convergence of the results with decreasing mesh size for all considered cases.

6 Application to a radome geometry

We analyze an ogive-shaped radome, which is a common design for a nose cone radome, see Figure 5. This design has several features of a realistic radome, in

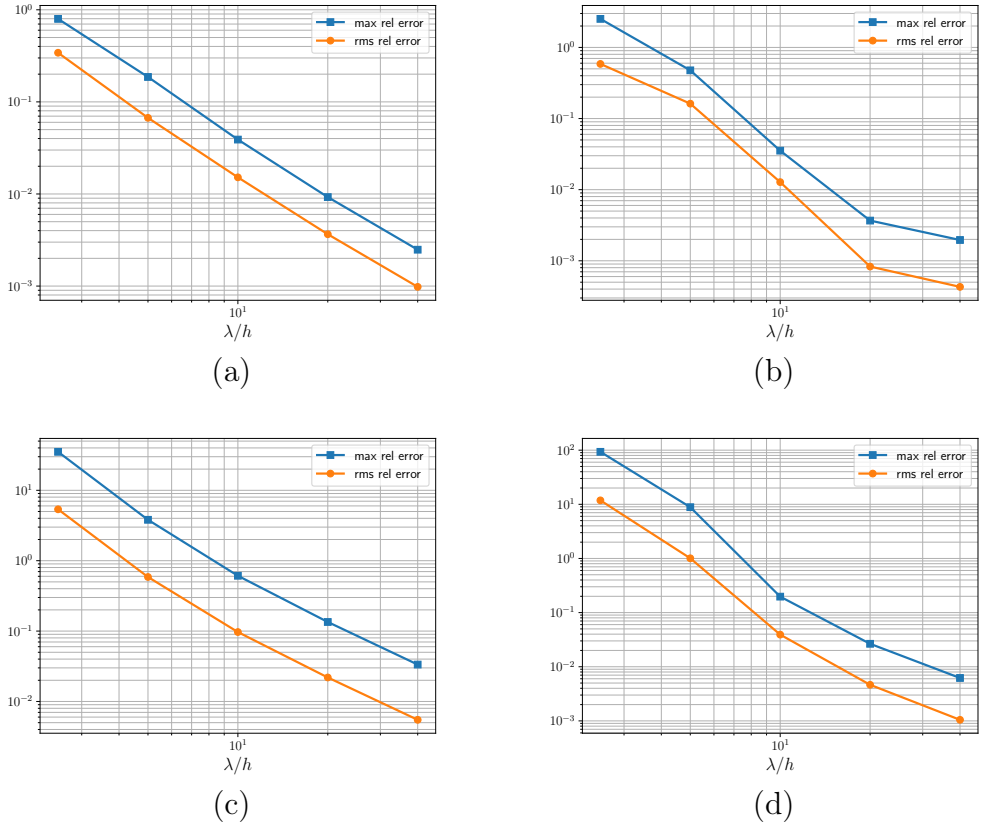

Figure 4: Results for h-convergence of H-plane differential scattering cross section of some spheres. (a) PEC sphere radius $\lambda/2$, (b) PEC sphere radius 3λ, (c) lossy dielectric sphere radius $\lambda/2$, (d) lossy dielectric sphere radius 3λ.

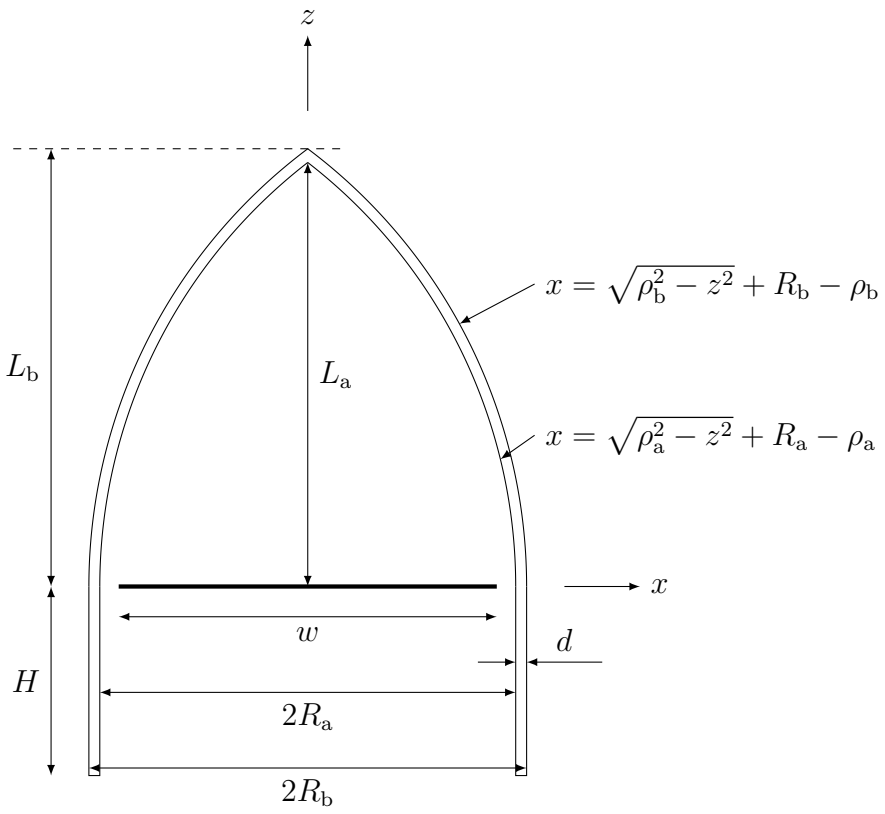

Figure 5: Geometry parameters of the ogive radome, adapted from https://en.wikipedia.org/wiki/Nose_cone_design. The radius of curvature for the ogive parts is computed from the other parameters as $\rho_{a,b} = (R_{a,b}^2 + L_{a,b}^2)/(2R_{a,b})$, and the thickness of the radome at the base is $d = R_b - R_a$. The antenna width is w, and the distance between the antenna and the radome is $d_0 = R_a - w/2$.

particular a pointed tip. The baseline parameters of the radome, corresponding to Figure 5, are chosen as

- $f_0 = 10\,\text{GHz}$ (frequency)
- $\lambda_0 = c/f_0$ (wavelength)
- $w = 10\lambda_0 = 0.300\,\text{m}$ (diameter of antenna)
- $d_0 = \lambda_0/2 = 0.0150\,\text{m}$ (distance from antenna to radome)
- $\epsilon_\text{r} = 3$ (relative permittivity of radome, lossless)
- $d = \lambda_0/(2\sqrt{\epsilon_\text{r}}) = 8.7\,\text{mm}$ (thickness of radome)
- $\alpha = 2$ (ogive shape factor)
- $R_\text{a} = w/2 + d_0 = 0.165\,\text{m}$
- $L_\text{a} = \alpha R_\text{a} = 0.330\,\text{m}$
- $\rho_\text{a} = (R_\text{a}^2 + L_\text{a}^2)/(2R_\text{a}) = 0.412\,\text{m}$
- $R_\text{b} = w/2 + d_0 + d = 0.174\,\text{m}$
- $L_\text{b} = \alpha R_\text{b} = 0.347\,\text{m}$
- $\rho_\text{b} = (R_\text{b}^2 + L_\text{b}^2)/(2R_\text{b}) = 0.434\,\text{m}$
- $H = 5\lambda_0 = 0.150\,\text{m}$

The antenna is implemented as a circular antenna with thickness $0.1\lambda_0$ and a cosine-tapering in the radial direction, that is, the antenna field is

$$\boldsymbol{E}_\text{a}(\boldsymbol{r}) = \boldsymbol{E}_0 \text{e}^{-\text{j}\boldsymbol{k}\cdot\boldsymbol{r}} \cos(\pi\rho/w), \quad \boldsymbol{r} \in \Gamma_\text{ant} \tag{6.1}$$

where the expression for a plane wave in (B.14) is used to express $\boldsymbol{E}_0 \text{e}^{-\text{j}\boldsymbol{k}\cdot\boldsymbol{r}}$ in azimuthal modes. The baseline antenna is ten wavelengths in diameter, making the radiation highly directive.

The excitation corresponding to an incident plane wave is $\boldsymbol{E}_\text{b}(\boldsymbol{r}) = \boldsymbol{E}_0 \text{e}^{-\text{j}\boldsymbol{k}\cdot\boldsymbol{r}}$. In both the antenna excitation and the plane wave excitation, the azimuth modes are found from the expressions in Appendix B.

6.1 Parameter variations

From the baseline geometry we make a number of parameter variations in the simulations:

- Electric field in θ (TM, in plane) or ϕ (TE, out of plane) polarization.
- Angle of incidence $\theta \in [0°, 10°, 20°, 30°, 40°, 50°]$.

- With and without radome.
- Either with a transmitting antenna or scattering from an incident plane wave.
- Antenna width $w \in [10\lambda_0, 20\lambda_0, 30\lambda_0]$. Note that the radome thickness is $\lambda_0/(2\sqrt{\epsilon_r})$ in all cases, that is, the radome is always transparent.

All combinations of these parameters have been run, and the results are discussed in the following subsection. The mesh size was chosen as $h = \lambda_0/10$, and the structure was surrounded by a cylindrical PML with thickness $\lambda_0/2$ at distance λ_0 from the radome in all directions.

6.2 Results

Typical examples of near field plots are given in Figure 6, where the scattered field is plotted for a plane wave excitation, and the total field is plotted for a transmitting antenna excitation. The results are given for three different radome sizes, corresponding to antenna widths $w = 10\lambda_0, 20\lambda_0, 30\lambda_0$, using ϕ-polarization.

For the incident plane wave (top row), it is seen there is a significant scattered field inside the radome cavity; this is due to the delay through the radome wall, and does not necessarily mean the radome scatters in the monostatic direction. There is also a strong scattered field in the region beneath the antenna, which is necessary to cancel the incident field in this shadow region. Some significant scattering is observed near the pointed tip of the radome, especially for the larger radome.

For the transmitting case, we can clearly see a reflection lobe travelling to the left. This is due to imperfect transmission of the wave through the radome wall, which was designed with normal incidence in mind. The curvature of the radome further shapes this reflection lobe.

Far field results in the plane of incidence for an incident plane wave are shown in Figure 7 for antenna width $w = 10\lambda_0$. Both polarizations and the cases with and without radome are reported. It is seen that there is a significantly increased bistatic scattering at some angles for the ϕ-polarization when the radome is present, whereas the corresponding effect is smaller for the θ-polarization.

In Figure 8, the corresponding results are plotted for the transmitting antenna excitation. Here, we observe significantly increased and broad side lobe levels with the radome present, for both polarizations. This is the reflection lobe earlier observed in the near field plots in Figure 6, due to imperfect transmission through the radome wall. A somewhat increased side lobe around $-40°$ can be observed in the ϕ-polarization without radome for high steering angles, in particular $\theta = 40°$. This indicates there is some scattering occurring at the edges of the antenna for this polarization, even without the radome present.

Figures 9 and 11 show the same results as Figure 7 but for antenna widths $w = 20\lambda_0$ and $30\lambda_0$, respectively. It is seen that the trend of increased side lobes for the ϕ-polarization is maintained for the larger radome sizes, with a more moderate increase for the θ-polarization.

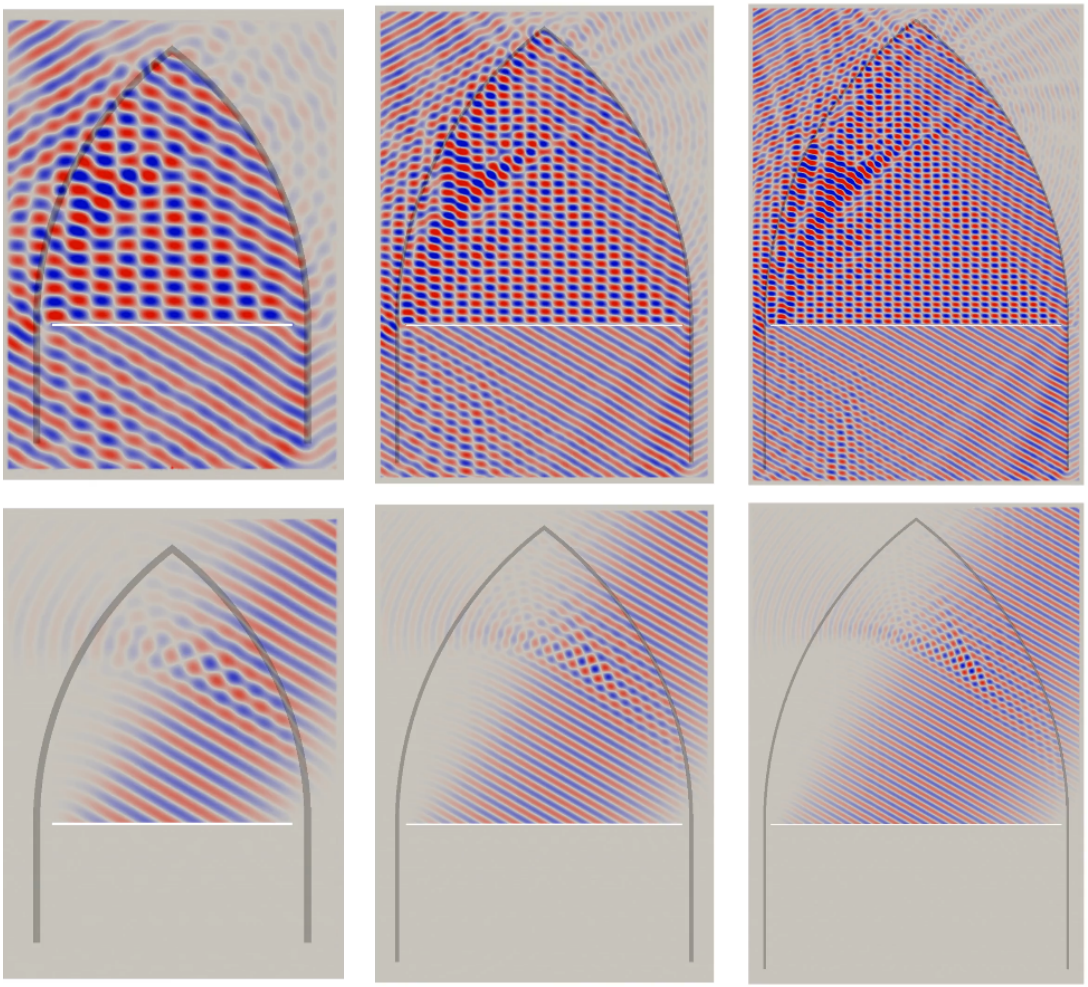

Figure 6: Near field plots of scattered field when subjected to an incident plane wave from $\theta = 30^\circ$ (top row) and total field with transmitting antenna towards $\theta = 30^\circ$ (bottom row) from antenna with radome present, antenna widths $w = 10\lambda_0, 20\lambda_0, 30\lambda_0$ (from left to right).

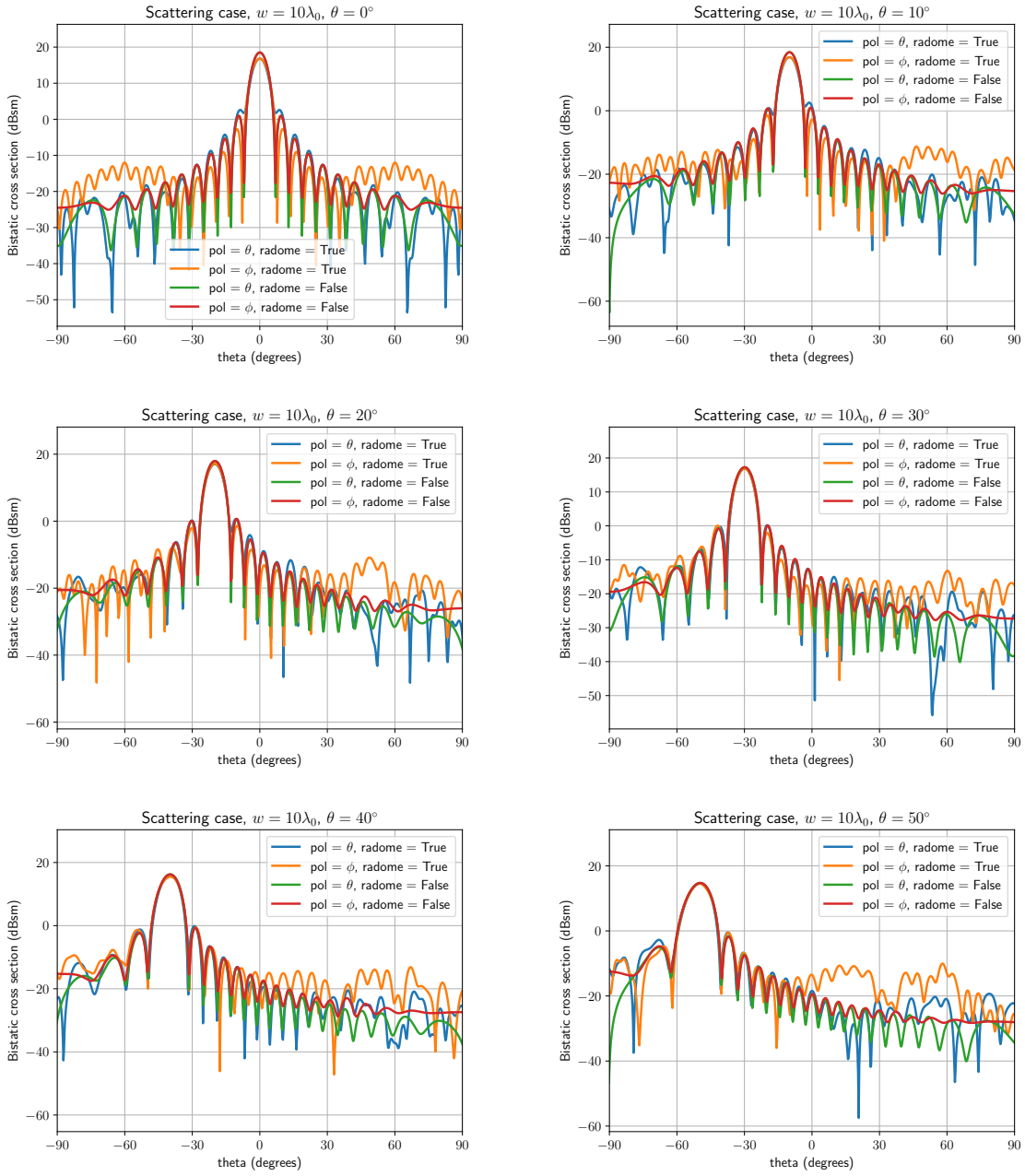

Figure 7: Scattering from antenna with and without radome, antenna width $w = 10\lambda_0$.

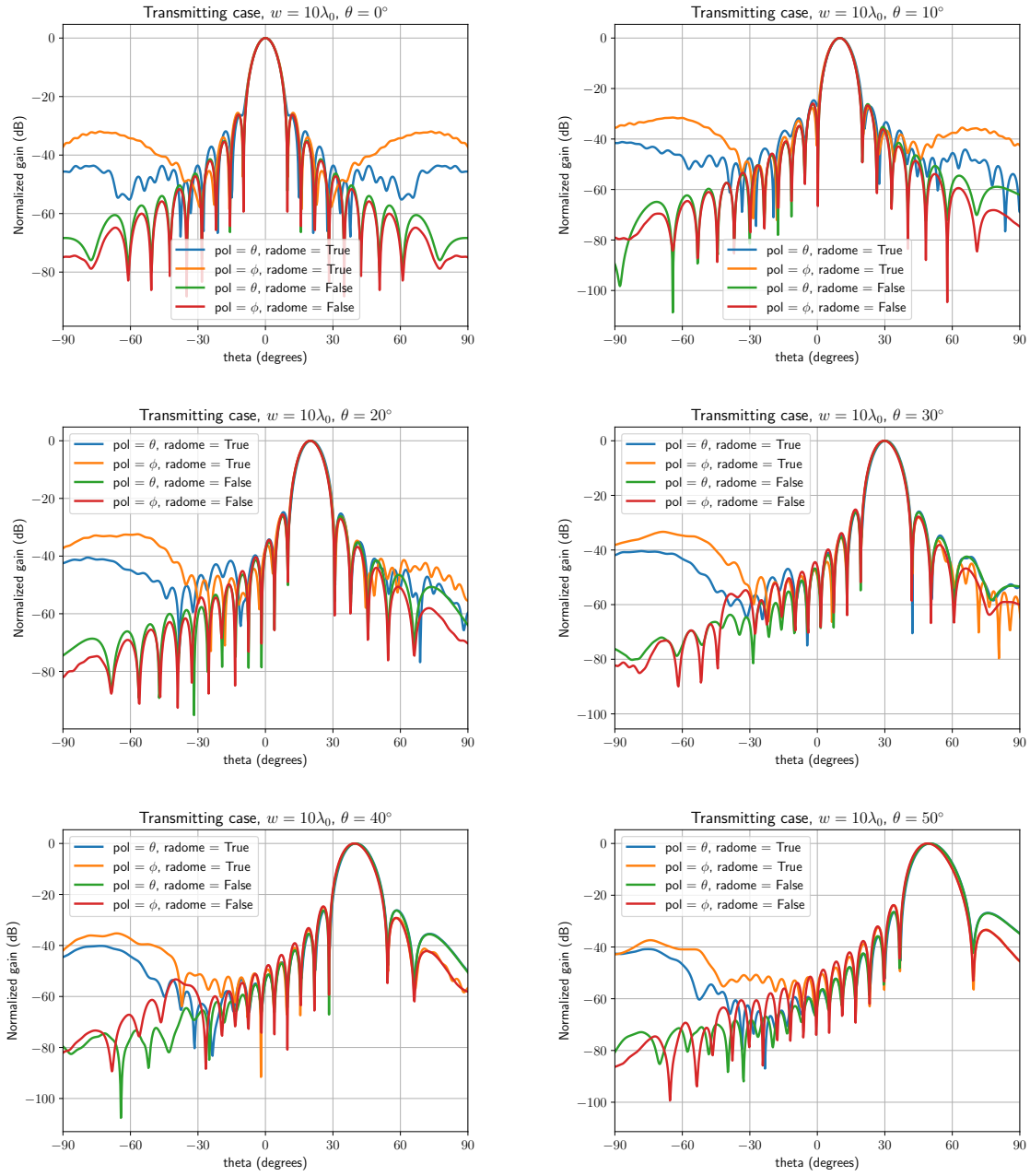

Figure 8: Transmission from antenna with and without radome, antenna width $w = 10\lambda_0$.

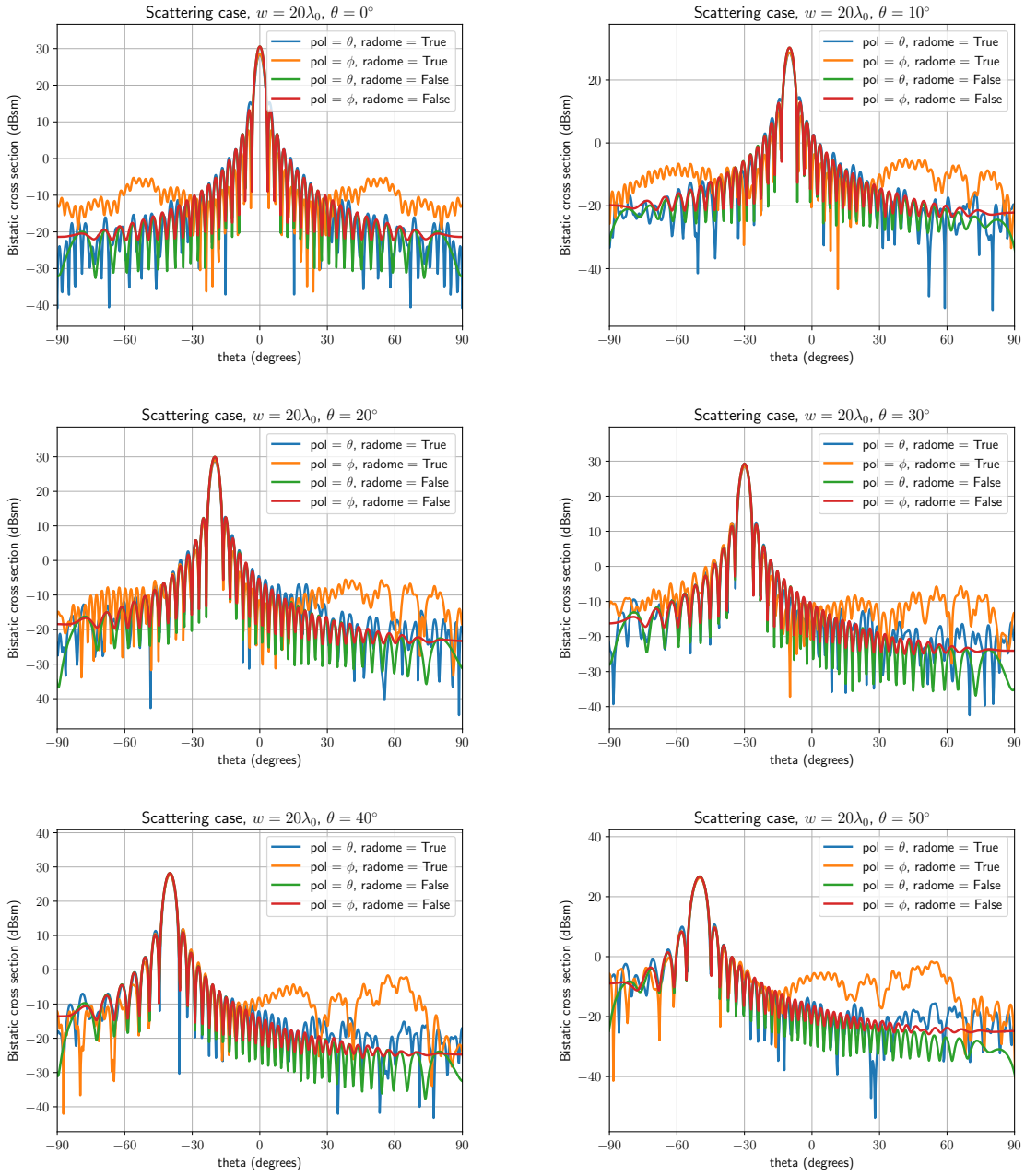

Figure 9: Scattering from antenna with and without radome, antenna width $w = 20\lambda_0$.

Finally, Figures 10 and 12 show the same results for a transmitting antenna as Figure 8 but for antenna widths $w = 20\lambda_0$ and $30\lambda_0$, respectively. The reflection lobe is clearly visible in both polarizations when the radome is present. Also, the increased side lobe for the ϕ-polarization without radome remains, in particular for $w = 30\lambda_0$ at $\theta = 40°$ and $50°$.

7 Conclusions

We have described the theory and implementation of a finite elements code for the simulation of a rotationally symmetric geometry, with the purpose to provide benchmark cases for large radome simulations. The code has been verified using scattering against PEC spheres and lossy dielectric spheres using a Mie scattering code. The code can handle excitation both with a transmitting antenna (with or without a tapering for low side lobes), and an incident plane wave, with arbitrary polarization. Both far field and near field data can be considered, where the far field data can also be projected on the spherical vector harmonics.

An application case has been illustrated, where a simple ogive-shaped half-wavelength radome in various sizes has been simulated. An increased bistatic scattering was observed for an incident plane wave of ϕ-polarization, and a reflection lobe in the transmitting case was observed in both near field and far field data for both polarizations. It should be emphasized that the radome studied has not been optimized in any way, and the results presented here are only intended to provide a reference case for other codes, not to represent a good design.

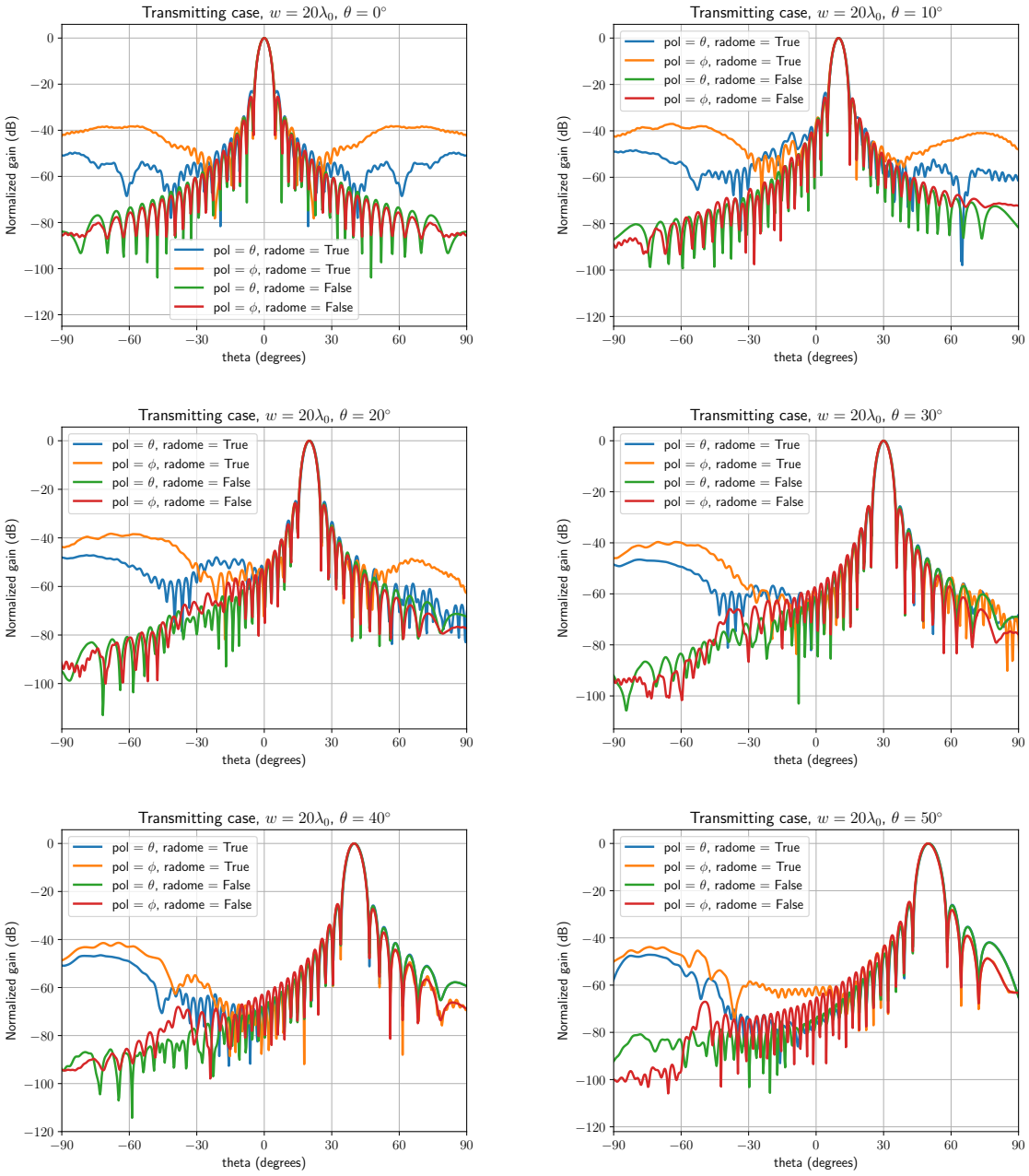

Figure 10: Transmission from antenna with and without radome, antenna width $w = 20\lambda_0$.

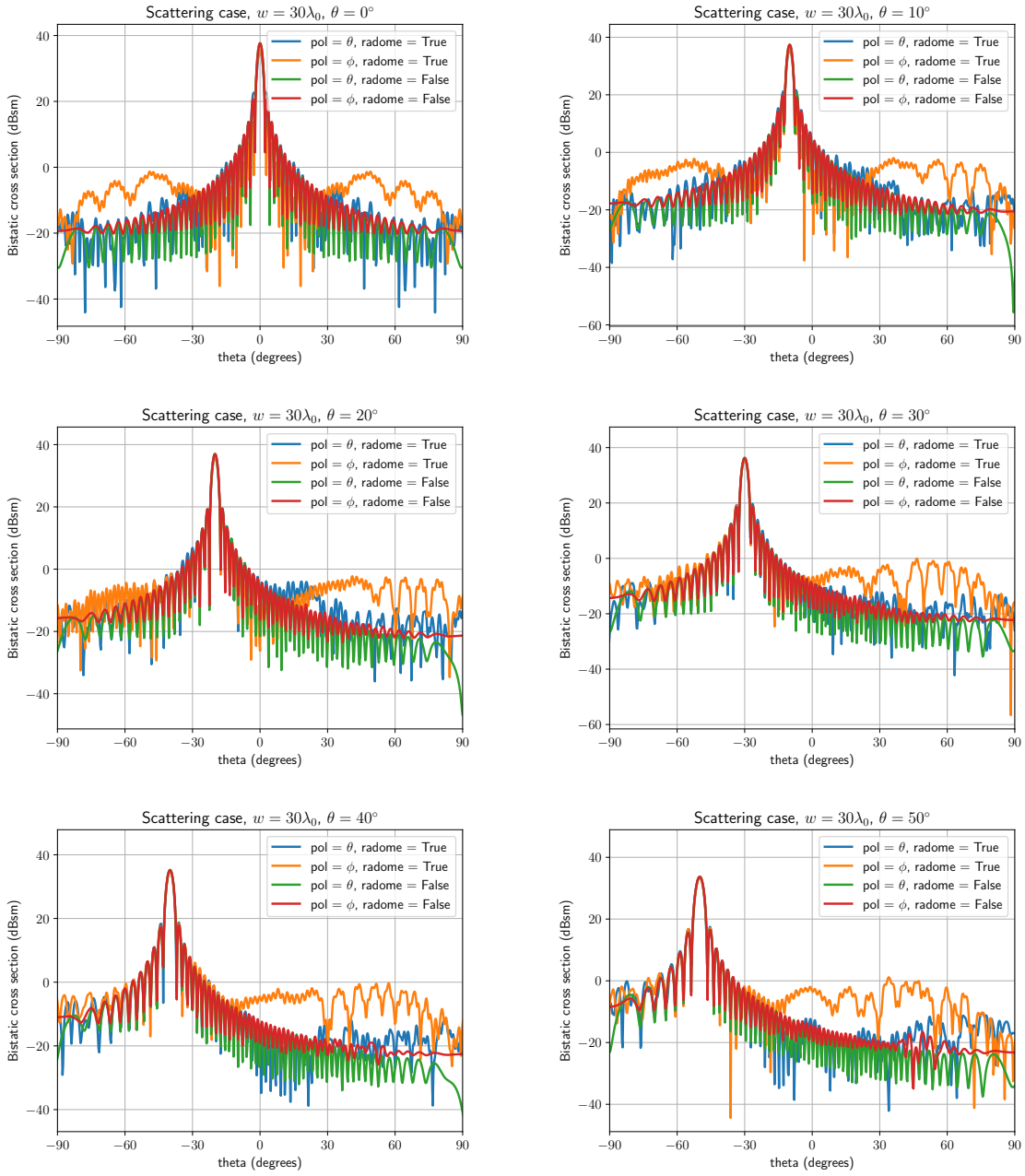

Figure 11: Scattering from antenna with and without radome, antenna width $w = 30\lambda_0$.

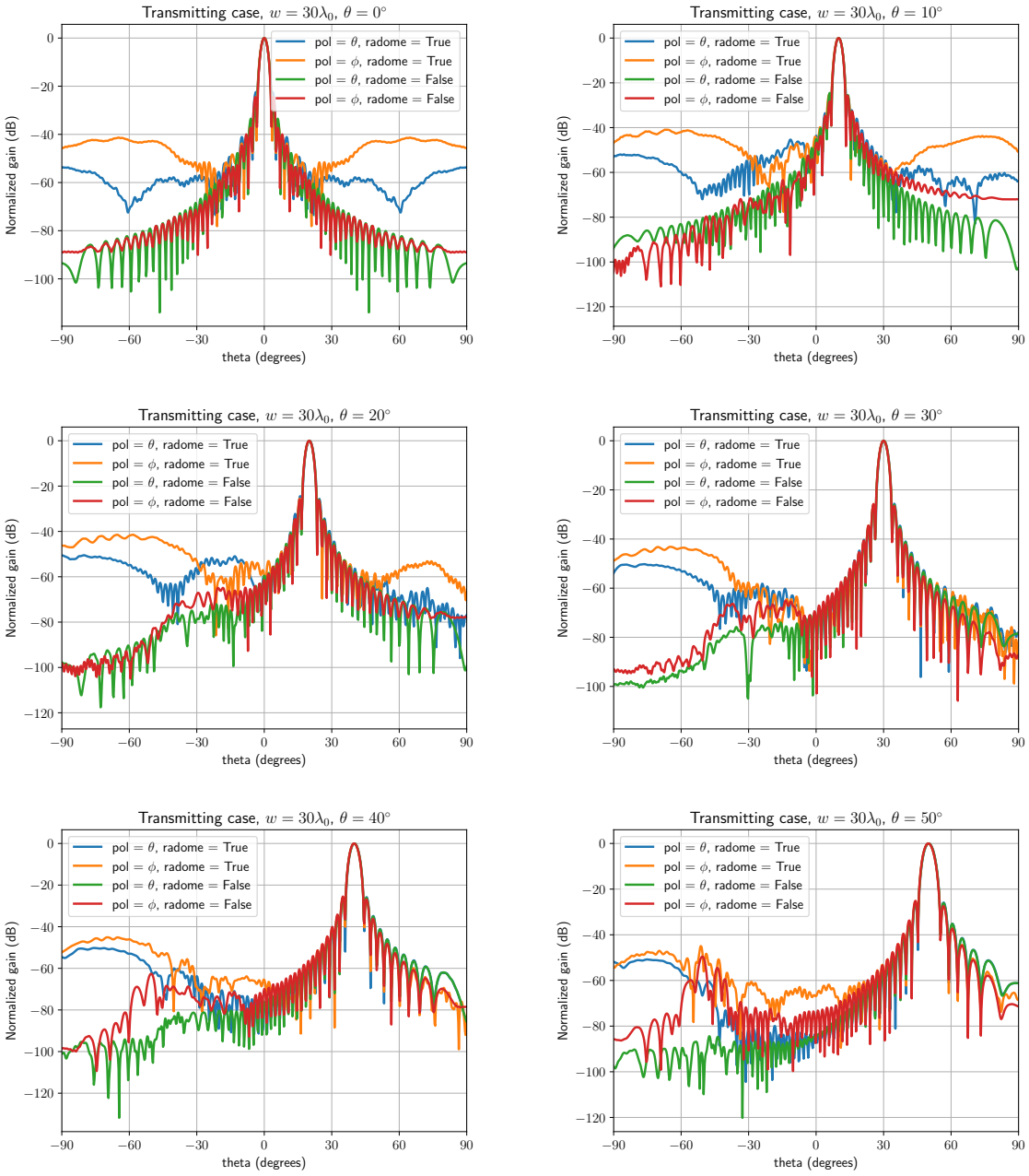

Figure 12: Transmission from antenna with and without radome, antenna width $w = 30\lambda_0$.

A Perfectly matched layer

A perfectly matched layer (PML) region is used to absorb the outgoing scattered field. We follow the dolfinx v0.7 demo on axisymmetric scattering,[1] and consider a spherical region with stretched cylindrical coordinates $\rho'(\rho, z)$, $z'(\rho, z)$, and $\varphi' = \varphi$. The coordinate transformation has the Jacobian

$$\mathbf{J} = \mathbf{A}^{-1} = \nabla \boldsymbol{r}'(\boldsymbol{r}) = \begin{pmatrix} \frac{\partial \rho'}{\partial \rho} & \frac{\partial z'}{\partial \rho} & 0 \\ \frac{\partial \rho'}{\partial z} & \frac{\partial z'}{\partial z} & 0 \\ 0 & 0 & \frac{\rho'}{\rho}\frac{\partial \varphi'}{\partial \varphi} \end{pmatrix}, \tag{A.1}$$

and the PML material parameters are (with $A = \det(\mathbf{A})$)

$$\boldsymbol{\epsilon}_{\mathrm{r,pml}} = A^{-1}\mathbf{A}\boldsymbol{\epsilon}_{\mathrm{b}}\mathbf{A}^{\mathrm{T}} \tag{A.2}$$

$$\boldsymbol{\mu}_{\mathrm{r,pml}} = A^{-1}\mathbf{A}\boldsymbol{\mu}_{\mathrm{b}}\mathbf{A}^{\mathrm{T}}. \tag{A.3}$$

We consider stretching with a polynomial profile in spherical radius $r = \sqrt{\rho^2 + z^2}$ such that [17, p. 663]

$$\rho' = \rho\left(1 - \mathrm{j}\frac{(n+1)\ln(1/R_0)}{2k(r_{\mathrm{pml}} - r_{\mathrm{dom}})}\left(\frac{r - r_{\mathrm{dom}}}{r_{\mathrm{pml}} - r_{\mathrm{dom}}}\right)^n\right) \tag{A.4}$$

$$z' = z\left(1 - \mathrm{j}\frac{(n+1)\ln(1/R_0)}{2k(r_{\mathrm{pml}} - r_{\mathrm{dom}})}\left(\frac{r - r_{\mathrm{dom}}}{r_{\mathrm{pml}} - r_{\mathrm{dom}}}\right)^n\right). \tag{A.5}$$

where R_0 is the desired (amplitude scale) reflection coefficient at normal incidence, and n is the polynomial order. Suitable choices are $R_0 = 10^{-10}$ and $n = 3$.

Another option is to stretch coordinates in ρ and z independently, which allows for structures parallel to the z-axis extending into the PML (and hence considered infinite in this direction). This is obtained by

$$\rho' = \rho\left(1 - \mathrm{j}\frac{(n+1)\ln(1/R_0)}{2k(\rho_{\mathrm{pml}} - \rho_{\mathrm{dom}})}\left(\frac{\rho - \rho_{\mathrm{dom}}}{\rho_{\mathrm{pml}} - \rho_{\mathrm{dom}}}\right)^n\right) \qquad \rho_{\mathrm{dom}} < \rho < \rho_{\mathrm{pml}} \tag{A.6}$$

$$z' = z\left(1 - \mathrm{j}\frac{(n+1)\ln(1/R_0)}{2k(z_{\mathrm{pml,t}} - z_{\mathrm{dom,t}})}\left(\frac{z - z_{\mathrm{dom,t}}}{z_{\mathrm{pml,t}} - z_{\mathrm{dom,t}}}\right)^n\right) \qquad z_{\mathrm{dom,t}} < z < z_{\mathrm{pml,t}} \tag{A.7}$$

$$z' = z\left(1 - \mathrm{j}\frac{(n+1)\ln(1/R_0)}{2k(z_{\mathrm{dom,b}} - z_{\mathrm{pml,b}})}\left(\frac{z_{\mathrm{dom,b}} - z}{z_{\mathrm{dom,b}} - z_{\mathrm{pml,b}}}\right)^n\right) \qquad z_{\mathrm{pml,b}} < z < z_{\mathrm{dom,b}} \tag{A.8}$$

and unstretched coordinates otherwise. In the overlap regions, both ρ' and z' are stretched by the formulas above. We can write a stretching function (note the use of the absolute value in order to have positive quantities regardless of the sign of $x_{\mathrm{pml}} - x_{\mathrm{dom}}$)

$$s(x, x_{\mathrm{dom}}, x_{\mathrm{pml}}) = 1 - \mathrm{j}\frac{(n+1)\ln(1/R_0)}{2k|x_{\mathrm{pml}} - x_{\mathrm{dom}}|}\left(\frac{x - x_{\mathrm{dom}}}{x_{\mathrm{pml}} - x_{\mathrm{dom}}}\right)^n, \tag{A.9}$$

[1] https://docs.fenicsproject.org/dolfinx/main/python/demos/demo_axis.html

where x denotes the coordinate normal to the PML, with x_{dom} and x_{pml} denoting the coordinates at the end of the domain and the end of the PML, respectively. Hence, a spherical PML has

$$\rho' = \rho s(r, r_{\mathrm{dom}}, r_{\mathrm{pml}}) \qquad r_{\mathrm{dom}} < r < r_{\mathrm{pml}} \tag{A.10}$$
$$z' = z s(r, r_{\mathrm{dom}}, r_{\mathrm{pml}}) \qquad r_{\mathrm{dom}} < r < r_{\mathrm{pml}} \tag{A.11}$$

with $r = \sqrt{\rho^2 + z^2}$, whereas a cylindrical PML has

$$\rho' = \rho s(\rho, \rho_{\mathrm{dom}}, \rho_{\mathrm{pml}}) \qquad \rho_{\mathrm{dom}} < \rho < \rho_{\mathrm{pml}} \tag{A.12}$$
$$z' = z s(z, z_{\mathrm{dom,t}}, z_{\mathrm{pml,t}}) \qquad z_{\mathrm{dom,t}} < z < z_{\mathrm{pml,t}} \tag{A.13}$$
$$z' = z s(z, z_{\mathrm{dom,b}}, z_{\mathrm{pml,b}}) \qquad z_{\mathrm{pml,t}} < z < z_{\mathrm{dom,t}}. \tag{A.14}$$

We note that this is not strictly the correct scaling since s depends on the coordinates, we should have $s = \partial\rho'/\partial\rho$ etc. However, it seems to work in practice.

B Plane wave in cylindrical coordinates

An incident plane wave is described by

$$\boldsymbol{E}_{\mathrm{b}}(\boldsymbol{r}) = \boldsymbol{E}_0 \mathrm{e}^{-\mathrm{j}\boldsymbol{k}\cdot\boldsymbol{r}}, \tag{B.1}$$

where

$$\boldsymbol{k} = k(\hat{\boldsymbol{x}} \sin\theta\cos\phi + \hat{\boldsymbol{y}} \sin\theta\sin\phi + \hat{\boldsymbol{z}}\cos\theta), \tag{B.2}$$

The Cartesian unit vectors can be written in terms of the cylindrical as

$$\hat{\boldsymbol{x}} = \hat{\boldsymbol{\rho}}\cos\varphi - \hat{\boldsymbol{\varphi}}\sin\varphi \tag{B.3}$$
$$\hat{\boldsymbol{y}} = \hat{\boldsymbol{\rho}}\sin\varphi + \hat{\boldsymbol{\varphi}}\cos\varphi \tag{B.4}$$
$$\hat{\boldsymbol{z}} = \hat{\boldsymbol{z}}, \tag{B.5}$$

implying

$$\boldsymbol{k}\cdot\boldsymbol{r} = k\rho\sin\theta(\cos\phi\cos\varphi + \sin\phi\sin\varphi) + kz\cos\theta = k\rho\sin\theta\cos(\varphi-\phi) + kz\cos\theta. \tag{B.6}$$

Using the Jacobi-Anger expansion [1, pp. 9.1.42–45]

$$\mathrm{e}^{\mathrm{j}z\cos\varphi} = \sum_{n=-\infty}^{\infty} \mathrm{j}^n \,\mathrm{J}_n(z)\mathrm{e}^{\mathrm{j}n\varphi}, \tag{B.7}$$

we can then write

$$\mathrm{e}^{-\mathrm{j}\boldsymbol{k}\cdot\boldsymbol{r}} = \mathrm{e}^{-\mathrm{j}k\rho\sin\theta\cos(\varphi-\phi)}\mathrm{e}^{-\mathrm{j}kz\cos\theta} = \mathrm{e}^{-\mathrm{j}kz\cos\theta}\sum_{n=-\infty}^{\infty}(-\mathrm{j})^n\,\mathrm{J}_n(k\rho\sin\theta)\mathrm{e}^{-\mathrm{j}n(\varphi-\phi)}. \tag{B.8}$$

The polarization of the wave is

$$\boldsymbol{E}_0 = \hat{\boldsymbol{\theta}}E_\theta + \hat{\boldsymbol{\phi}}E_\phi, \tag{B.9}$$

where the unit vectors are

$$\begin{aligned}\hat{\boldsymbol{\theta}} &= \cos\theta\cos\phi\hat{\boldsymbol{x}} + \cos\theta\sin\phi\hat{\boldsymbol{y}} - \sin\theta\hat{\boldsymbol{z}} \\ &= \cos\theta(\cos\phi\cos\varphi + \sin\phi\sin\varphi)\hat{\boldsymbol{\rho}} + \cos\theta(-\cos\phi\sin\varphi + \sin\phi\cos\varphi)\hat{\boldsymbol{\varphi}} - \sin\theta\hat{\boldsymbol{z}} \\ &= \cos\theta\cos(\varphi-\phi)\hat{\boldsymbol{\rho}} - \cos\theta\sin(\varphi-\phi)\hat{\boldsymbol{\varphi}} - \sin\theta\hat{\boldsymbol{z}} \quad \text{(B.10)}\end{aligned}$$

and

$$\begin{aligned}\hat{\boldsymbol{\phi}} &= -\sin\phi\hat{\boldsymbol{x}} + \cos\phi\hat{\boldsymbol{y}} = (-\sin\phi\cos\varphi + \cos\phi\sin\varphi)\hat{\boldsymbol{\rho}} + (\sin\phi\sin\varphi + \cos\phi\cos\varphi)\hat{\boldsymbol{\varphi}} \\ &= \sin(\varphi-\phi)\hat{\boldsymbol{\rho}} + \cos(\varphi-\phi)\hat{\boldsymbol{\varphi}}. \quad \text{(B.11)}\end{aligned}$$

Using Euler's formula we have

$$\cos(\varphi-\phi) = \frac{\mathrm{e}^{\mathrm{j}(\varphi-\phi)} + \mathrm{e}^{-\mathrm{j}(\varphi-\phi)}}{2} \quad \text{and} \quad \sin(\varphi-\phi) = \frac{\mathrm{e}^{\mathrm{j}(\varphi-\phi)} - \mathrm{e}^{-\mathrm{j}(\varphi-\phi)}}{2\mathrm{j}}, \quad \text{(B.12)}$$

and the final version of the plane wave expansion is

$$\begin{aligned}\boldsymbol{E}_0\mathrm{e}^{-\mathrm{j}\boldsymbol{k}\cdot\boldsymbol{r}} = E_\theta\mathrm{e}^{-\mathrm{j}kz\cos\theta}\Bigg\{ &\left[\sum_{n=-\infty}^{\infty}(-\mathrm{j})^n\,\mathrm{J}_n(k\rho\sin\theta)\frac{1}{2}(\mathrm{e}^{-\mathrm{j}(n-1)(\varphi-\phi)} + \mathrm{e}^{-\mathrm{j}(n+1)(\varphi-\phi)})\right]\cos\theta\hat{\boldsymbol{\rho}} \\ &+ \left[\sum_{n=-\infty}^{\infty}(-\mathrm{j})^n\,\mathrm{J}_n(k\rho\sin\theta)\frac{1}{2\mathrm{j}}(\mathrm{e}^{-\mathrm{j}(n-1)(\varphi-\phi)} - \mathrm{e}^{-\mathrm{j}(n+1)(\varphi-\phi)})\right](-\cos\theta)\hat{\boldsymbol{\varphi}} \\ &+ \left[\sum_{n=-\infty}^{\infty}(-\mathrm{j})^n\,\mathrm{J}_n(k\rho\sin\theta)\mathrm{e}^{-\mathrm{j}n(\varphi-\phi)}\right](-\sin\theta)\hat{\boldsymbol{z}}\Bigg\} \\ + E_\phi\mathrm{e}^{-\mathrm{j}kz\cos\theta}\Bigg\{ &\left[\sum_{n=-\infty}^{\infty}(-\mathrm{j})^n\,\mathrm{J}_n(k\rho\sin\theta)\frac{1}{2\mathrm{j}}(\mathrm{e}^{-\mathrm{j}(n-1)(\varphi-\phi)} - \mathrm{e}^{-\mathrm{j}(n+1)(\varphi-\phi)})\right]\hat{\boldsymbol{\rho}} \\ &+ \left[\sum_{n=-\infty}^{\infty}(-\mathrm{j})^n\,\mathrm{J}_n(k\rho\sin\theta)\frac{1}{2}(\mathrm{e}^{-\mathrm{j}(n-1)(\varphi-\phi)} + \mathrm{e}^{-\mathrm{j}(n+1)(\varphi-\phi)})\right]\hat{\boldsymbol{\varphi}}\Bigg\}. \quad \text{(B.13)}\end{aligned}$$

Rewriting in terms of azimuthal modes, we find

$$\begin{aligned}\boldsymbol{E}_0\mathrm{e}^{-\mathrm{j}\boldsymbol{k}\cdot\boldsymbol{r}} = E_\theta\mathrm{e}^{-\mathrm{j}kz\cos\theta}\Bigg\{ &\sum_{n=-\infty}^{\infty}\frac{1}{2}\left[(-\mathrm{j})^{n+1}\,\mathrm{J}_{n+1}(k\rho\sin\theta) + (-\mathrm{j})^{n-1}\,\mathrm{J}_{n-1}(k\rho\sin\theta)\right]\mathrm{e}^{-\mathrm{j}n(\varphi-\phi)}\cos\theta\hat{\boldsymbol{\rho}} \\ &+ \sum_{n=-\infty}^{\infty}\frac{1}{2\mathrm{j}}\left[(-\mathrm{j})^{n+1}\,\mathrm{J}_{n+1}(k\rho\sin\theta) - (-\mathrm{j})^{n-1}\,\mathrm{J}_{n-1}(k\rho\sin\theta)\right]\mathrm{e}^{-\mathrm{j}n(\varphi-\phi)}(-\cos\theta)\hat{\boldsymbol{\varphi}} \\ &+ \sum_{n=-\infty}^{\infty}(-\mathrm{j})^n\,\mathrm{J}_n(k\rho\sin\theta)\mathrm{e}^{-\mathrm{j}n(\varphi-\phi)}(-\sin\theta)\hat{\boldsymbol{z}}\Bigg\} \\ + E_\phi\mathrm{e}^{-\mathrm{j}kz\cos\theta}\Bigg\{ &\sum_{n=-\infty}^{\infty}\frac{1}{2\mathrm{j}}\left[(-\mathrm{j})^{n+1}\,\mathrm{J}_{n+1}(k\rho\sin\theta) - (-\mathrm{j})^{n-1}\,\mathrm{J}_{n-1}(k\rho\sin\theta)\right]\mathrm{e}^{-\mathrm{j}n(\varphi-\phi)}\hat{\boldsymbol{\rho}} \\ &+ \sum_{n=-\infty}^{\infty}\frac{1}{2}\left[(-\mathrm{j})^{n+1}\,\mathrm{J}_{n+1}(k\rho\sin\theta) + (-\mathrm{j})^{n-1}\,\mathrm{J}_{n-1}(k\rho\sin\theta)\right]\mathrm{e}^{-\mathrm{j}n(\varphi-\phi)}\hat{\boldsymbol{\varphi}}\Bigg\}, \quad \text{(B.14)}\end{aligned}$$

which is our final expression. This expression can also be used to compute an antenna excitation $\boldsymbol{E}_{\mathrm{a}}$: simply evaluate it on the antenna surface, possibly multiplied by an amplitude taper.

C Computation of far field amplitudes

In this Appendix, we give explicit derivations of how the far field amplitudes used in the computational examples can be derived. The general setup of solving Maxwell's equations in a rotationally symmetric geometry is provided in Section 2. There, it is seen that the fields can be represented in cylindrical coordinates (ρ, φ, z) as

$$\boldsymbol{E}(\boldsymbol{r}) = \sum_{m=-\infty}^{\infty} \left[E_\rho^{(m)}(\rho,z)\hat{\boldsymbol{\rho}} + E_\varphi^{(m)}(\rho,z)\hat{\boldsymbol{\varphi}} + E_z^{(m)}(\rho,z)\hat{\boldsymbol{z}}\right] \mathrm{e}^{-\mathrm{j}m\varphi} \tag{C.1}$$

$$\boldsymbol{H}(\boldsymbol{r}) = \sum_{m=-\infty}^{\infty} \left[H_\rho^{(m)}(\rho,z)\hat{\boldsymbol{\rho}} + H_\varphi^{(m)}(\rho,z)\hat{\boldsymbol{\varphi}} + H_z^{(m)}(\rho,z)\hat{\boldsymbol{z}}\right] \mathrm{e}^{-\mathrm{j}m\varphi}. \tag{C.2}$$

In this Appendix, we demonstrate how to solve the azimuthal part of the far field integral

$$\boldsymbol{F}(\hat{\boldsymbol{k}}) = \frac{\mathrm{j}k}{4\pi}\hat{\boldsymbol{k}} \times \iint_S \left[\boldsymbol{E}(\boldsymbol{r}) \times \hat{\boldsymbol{n}} + \eta_0 \hat{\boldsymbol{k}} \times (\hat{\boldsymbol{n}} \times \boldsymbol{H}(\boldsymbol{r}))\right] \mathrm{e}^{\mathrm{j}k\hat{\boldsymbol{k}}\cdot\boldsymbol{r}} \,\mathrm{d}S \tag{C.3}$$

for arbitrary azimuthal mode index m. The radiation direction $\hat{\boldsymbol{k}}$ is parameterized by the standard polar angle θ and azimuth angle ϕ.

The fields $\boldsymbol{E}^{(m)}(\rho,z)$ and $\boldsymbol{H}^{(m)}(\rho,z)$ depend only on ρ and z, whereas the φ-dependence is in a factor $\mathrm{e}^{-\mathrm{j}m\varphi}$. Hence, the far field integrals to be computed are proportional to

$$\int_{\boldsymbol{\rho}\in\gamma}\int_{\varphi=0}^{2\pi} [\boldsymbol{E}^{(m)} \times \hat{\boldsymbol{n}}]\mathrm{e}^{\mathrm{j}(\boldsymbol{k}\cdot\boldsymbol{r}-m\varphi)}\rho \,\mathrm{d}\varphi \,\mathrm{d}\ell \quad \text{and} \quad \int_{\boldsymbol{\rho}\in\gamma}\int_{\varphi=0}^{2\pi} [\hat{\boldsymbol{n}} \times \boldsymbol{H}^{(m)}]\mathrm{e}^{\mathrm{j}(\boldsymbol{k}\cdot\boldsymbol{r}-m\varphi)}\rho \,\mathrm{d}\varphi \,\mathrm{d}\ell, \tag{C.4}$$

where γ is the curve in the ρ-z plane where the integral is to be computed, ρ and z are coordinates on this curve, with $\mathrm{d}\ell$ as a line element. The unit normal vector is $\hat{\boldsymbol{n}} = n_\rho\hat{\boldsymbol{\rho}} + n_z\hat{\boldsymbol{z}}$, meaning the electric and magnetic tangential fields are (using $\hat{\boldsymbol{\rho}} \times \hat{\boldsymbol{\varphi}} = \hat{\boldsymbol{z}}$)

$$\boldsymbol{E}^{(m)} \times \hat{\boldsymbol{n}} = (n_\rho E_z^{(m)} - n_z E_\rho^{(m)})\hat{\boldsymbol{\varphi}} - n_\rho E_\varphi^{(m)}\hat{\boldsymbol{z}} + n_z E_\varphi^{(m)}\hat{\boldsymbol{\rho}} \tag{C.5}$$

$$\hat{\boldsymbol{n}} \times \boldsymbol{H}^{(m)} = (-n_\rho H_z^{(m)} + n_z H_\rho^{(m)})\hat{\boldsymbol{\varphi}} + n_\rho H_\varphi^{(m)}\hat{\boldsymbol{z}} - n_z H_\varphi^{(m)}\hat{\boldsymbol{\rho}}. \tag{C.6}$$

The unit vectors are

$$\hat{\boldsymbol{\rho}} = \hat{\boldsymbol{x}}\cos\varphi + \hat{\boldsymbol{y}}\sin\varphi \tag{C.7}$$

$$\hat{\boldsymbol{\varphi}} = -\hat{\boldsymbol{x}}\sin\varphi + \hat{\boldsymbol{y}}\cos\varphi, \tag{C.8}$$

meaning the tangential fields are

$$\boldsymbol{E}^{(m)} \times \hat{\boldsymbol{n}} = [n_z E_\varphi^{(m)} \cos(\varphi) - (n_\rho E_z^{(m)} - n_z E_\rho^{(m)}) \sin(\varphi)]\hat{\boldsymbol{x}} \tag{C.9}$$

$$+ [n_z E_\varphi^{(m)} \sin(\varphi) + (n_\rho E_z^{(m)} - n_z E_\rho^{(m)}) \cos(\varphi)]\hat{\boldsymbol{y}} - n_\rho E_\varphi^{(m)} \hat{\boldsymbol{z}} \tag{C.10}$$

$$\hat{\boldsymbol{n}} \times \boldsymbol{H}^{(m)} = -[n_z H_\varphi^{(m)} \cos(\varphi) - (n_\rho H_z^{(m)} - n_z H_\rho^{(m)}) \sin(\varphi)]\hat{\boldsymbol{x}} \tag{C.11}$$

$$- [n_z H_\varphi^{(m)} \sin(\varphi) + (n_\rho H_z^{(m)} - n_z H_\rho^{(m)}) \cos(\varphi)]\hat{\boldsymbol{y}} + n_\rho H_\varphi^{(m)} \hat{\boldsymbol{z}}. \tag{C.12}$$

The phase factor is

$$\mathrm{e}^{\mathrm{j}(\boldsymbol{k}\cdot\boldsymbol{r} - m\varphi)} = \mathrm{e}^{\mathrm{j}(\boldsymbol{k}\cdot(\rho\hat{\boldsymbol{\rho}} + z\hat{\boldsymbol{z}}) - m\varphi)} = \mathrm{e}^{\mathrm{j}(k\rho \sin\theta \cos(\varphi - \phi) - m\varphi)} \mathrm{e}^{\mathrm{j}kz\cos\theta}, \tag{C.13}$$

where we used $\boldsymbol{k}\cdot\boldsymbol{r} = k\rho\sin\theta\cos(\varphi - \phi) + kz\cos\theta$, with $\boldsymbol{k} = k[\sin\theta(\cos\phi\hat{\boldsymbol{x}} + \sin\phi\hat{\boldsymbol{y}}) +$

$\cos\theta\hat{\boldsymbol{z}}$]. Thus, the typical azimuth integrals to be computed are:

$$\begin{aligned}
\int_0^{2\pi} \mathrm{e}^{\mathrm{j}(k\rho\sin\theta\cos(\varphi-\phi)-m\varphi)}\,\mathrm{d}\varphi &\overset{\varphi'=\varphi-\phi+\pi/2}{=} \int_0^{2\pi} \mathrm{e}^{\mathrm{j}(k\rho\sin\theta\cos(\varphi'-\pi/2)-m(\varphi'+\phi-\pi/2))}\,\mathrm{d}\varphi' \\
&= \mathrm{e}^{-\mathrm{j}m(\phi-\pi/2)} \int_{-\pi}^{\pi} \mathrm{e}^{\mathrm{j}(k\rho\sin\theta\sin(\varphi')-m\varphi')}\,\mathrm{d}\varphi' \\
&= \mathrm{e}^{-\mathrm{j}m\phi}\mathrm{j}^m 2\pi\,\mathrm{J}_m(k\rho\sin\theta) \\
&= 2\pi\mathrm{j}^m\mathrm{e}^{-\mathrm{j}m\phi}A_m \qquad \text{(C.14)} \\
\int_0^{2\pi} \sin(\varphi)\mathrm{e}^{\mathrm{j}(k\rho\cos(\varphi-\phi)-m\varphi}\,\mathrm{d}\varphi &= \frac{1}{2\mathrm{j}}\Bigg[\int_0^{2\pi} \mathrm{e}^{\mathrm{j}(k\rho\sin\theta\cos(\varphi-\phi)-(m-1)\varphi)}\,\mathrm{d}\varphi \\
&\quad - \int_0^{2\pi} \mathrm{e}^{\mathrm{j}(k\rho\sin\theta\cos(\varphi-\phi)-(m+1)\varphi)}\,\mathrm{d}\varphi\Bigg] \\
&= \frac{1}{2\mathrm{j}}\Big[\mathrm{e}^{-\mathrm{j}(m-1)\phi}\mathrm{j}^{m-1}2\pi\,\mathrm{J}_{m-1}(k\rho\sin\theta) \\
&\quad - \mathrm{e}^{-\mathrm{j}(m+1)\phi}\mathrm{j}^{m+1}2\pi\,\mathrm{J}_{m+1}(k\rho\sin\theta)\Big] \\
&= 2\pi\mathrm{j}^m\mathrm{e}^{-\mathrm{j}m\phi}\frac{1}{2\mathrm{j}}\left[\mathrm{e}^{\mathrm{j}\phi}\mathrm{j}^{-1}\,\mathrm{J}_{m-1}(k\rho\sin\theta) - \mathrm{e}^{-\mathrm{j}\phi}\mathrm{j}\,\mathrm{J}_{m+1}(k\rho\sin\theta)\right] \\
&= -2\pi\mathrm{j}^m\mathrm{e}^{-\mathrm{j}m\phi}\frac{1}{2}\left[\mathrm{e}^{\mathrm{j}\phi}\,\mathrm{J}_{m-1}(k\rho\sin\theta) + \mathrm{e}^{-\mathrm{j}\phi}\,\mathrm{J}_{m+1}(k\rho\sin\theta)\right] \\
&= -2\pi\mathrm{j}^m\mathrm{e}^{-\mathrm{j}m\phi}S_m \qquad \text{(C.15)} \\
\int_0^{2\pi} \cos(\varphi)\mathrm{e}^{\mathrm{j}k\rho\cos(\varphi-\phi)-m\varphi}\,\mathrm{d}\varphi &= \frac{1}{2}\Bigg[\int_0^{2\pi} \mathrm{e}^{\mathrm{j}(k\rho\sin\theta\cos(\varphi-\phi)-(m-1)\varphi)}\,\mathrm{d}\varphi \\
&\quad + \int_0^{2\pi} \mathrm{e}^{\mathrm{j}(k\rho\sin\theta\cos(\varphi-\phi)-(m+1)\varphi)}\,\mathrm{d}\varphi\Bigg] \\
&= \frac{1}{2}\Big[\mathrm{e}^{-\mathrm{j}(m-1)\phi}\mathrm{j}^{m-1}2\pi\,\mathrm{J}_{m-1}(k\rho\sin\theta) \\
&\quad + \mathrm{e}^{-\mathrm{j}(m+1)\phi}\mathrm{j}^{m+1}2\pi\,\mathrm{J}_{m+1}(k\rho\sin\theta)\Big] \\
&= 2\pi\mathrm{j}^m\mathrm{e}^{-\mathrm{j}m\phi}\frac{1}{2}\left[\mathrm{e}^{\mathrm{j}\phi}\mathrm{j}^{-1}\,\mathrm{J}_{m-1}(k\rho\sin\theta) + \mathrm{e}^{-\mathrm{j}\phi}\mathrm{j}\,\mathrm{J}_{m+1}(k\rho\sin\theta)\right] \\
&= -2\pi\mathrm{j}^m\mathrm{e}^{-\mathrm{j}m\phi}\frac{\mathrm{j}}{2}\left[\mathrm{e}^{\mathrm{j}\phi}\,\mathrm{J}_{m-1}(k\rho\sin\theta) - \mathrm{e}^{-\mathrm{j}\phi}\,\mathrm{J}_{m+1}(k\rho\sin\theta)\right] \\
&= -2\pi\mathrm{j}^m\mathrm{e}^{-\mathrm{j}m\phi}C_m, \qquad \text{(C.16)}
\end{aligned}$$

where we used the representation [1, p. 9.1.21]

$$\mathrm{J}_m(z) = \frac{1}{\pi}\int_0^{\pi} \cos(z\sin\theta - m\theta)\,\mathrm{d}\theta = \frac{1}{2\pi}\int_{-\pi}^{\pi} \mathrm{e}^{\mathrm{j}(z\sin\theta-m\theta)}\,\mathrm{d}\theta = \frac{1}{2\pi}\int_0^{2\pi} \mathrm{e}^{\mathrm{j}(z\sin\theta-m\theta)}\,\mathrm{d}\theta, \qquad \text{(C.17)}$$

where m is a positive integer or zero. Thus, after integration over φ, we have

(premultiplying with the factor $1/(2\pi \mathrm{j}^m \mathrm{e}^{\mathrm{j}(kz\cos\theta - m\phi)})$ for simplicity)

$$\begin{aligned}\frac{1}{2\pi \mathrm{j}^m \mathrm{e}^{\mathrm{j}(kz\cos\theta - m\phi)}} \int_0^{2\pi} [\boldsymbol{E}^{(m)} \times \hat{\boldsymbol{n}}] \mathrm{e}^{\mathrm{j}(\boldsymbol{k}\cdot\boldsymbol{r} - m\varphi)}\, \mathrm{d}\varphi \\ = -\left[n_z E_\varphi^{(m)} C_m - (n_\rho E_z^{(m)} - n_z E_\rho^{(m)}) S_m\right] \hat{\boldsymbol{x}} \\ - \left[n_z E_\varphi^{(m)} S_m + (n_\rho E_z^{(m)} - n_z E_\rho^{(m)}) C_m\right] \hat{\boldsymbol{y}} - n_\rho E_\varphi^{(m)} A_m \hat{\boldsymbol{z}}, \quad \text{(C.18)}\end{aligned}$$

and

$$\begin{aligned}\frac{1}{2\pi \mathrm{j}^m \mathrm{e}^{\mathrm{j}(k_z z - m\phi)}} \int_0^{2\pi} [\hat{\boldsymbol{n}} \times \boldsymbol{H}^{(m)}] \mathrm{e}^{\mathrm{j}(\boldsymbol{k}\cdot\boldsymbol{r} - m\varphi)}\, \mathrm{d}\varphi \\ = \left[n_z H_\varphi^{(m)} C_m - (n_\rho H_z^{(m)} - n_z H_\rho^{(m)}) S_m\right] \hat{\boldsymbol{x}} \\ + \left[n_z H_\varphi^{(m)} S_m + (n_\rho H_z^{(m)} - n_z H_\rho^{(m)}) C_m\right] \hat{\boldsymbol{y}} + n_\rho H_\varphi^{(m)} A_m \hat{\boldsymbol{z}}. \quad \text{(C.19)}\end{aligned}$$

The remaining cross products are (rewriting $\hat{\boldsymbol{x}}$, $\hat{\boldsymbol{y}}$, and $\hat{\boldsymbol{z}}$ in terms of (θ, ϕ) as the polar angle and azimuth angle in the direction $\hat{\boldsymbol{k}}$)

$$\hat{\boldsymbol{k}} \times \hat{\boldsymbol{x}} = \hat{\boldsymbol{k}} \times (\hat{\boldsymbol{k}} \sin\theta\cos\phi + \hat{\boldsymbol{\theta}} \cos\theta\cos\phi - \hat{\boldsymbol{\phi}} \sin\phi) = \hat{\boldsymbol{\phi}} \cos\theta\cos\phi + \hat{\boldsymbol{\theta}} \sin\phi \quad \text{(C.20)}$$

$$\hat{\boldsymbol{k}} \times \hat{\boldsymbol{y}} = \hat{\boldsymbol{k}} \times (\hat{\boldsymbol{k}} \sin\theta\sin\phi + \hat{\boldsymbol{\theta}} \cos\theta\sin\phi + \hat{\boldsymbol{\phi}} \cos\phi) = \hat{\boldsymbol{\phi}} \cos\theta\sin\phi - \hat{\boldsymbol{\theta}} \cos\phi \quad \text{(C.21)}$$

$$\hat{\boldsymbol{k}} \times \hat{\boldsymbol{z}} = \hat{\boldsymbol{k}} \times (\hat{\boldsymbol{k}} \cos\theta - \hat{\boldsymbol{\theta}} \sin\theta) = -\hat{\boldsymbol{\phi}} \sin\theta \quad \text{(C.22)}$$

$$\begin{aligned}\hat{\boldsymbol{k}} \times (\hat{\boldsymbol{k}} \times \hat{\boldsymbol{x}}) &= [\hat{\boldsymbol{k}}\hat{\boldsymbol{k}} - \mathbf{1}] \cdot (\hat{\boldsymbol{k}} \sin\theta\cos\phi + \hat{\boldsymbol{\theta}} \cos\theta\cos\phi - \hat{\boldsymbol{\phi}} \sin\phi) \\ &= -\hat{\boldsymbol{\theta}} \cos\theta\cos\phi + \hat{\boldsymbol{\phi}} \sin\phi \quad \text{(C.23)}\end{aligned}$$

$$\begin{aligned}\hat{\boldsymbol{k}} \times (\hat{\boldsymbol{k}} \times \hat{\boldsymbol{y}}) &= [\hat{\boldsymbol{k}}\hat{\boldsymbol{k}} - \mathbf{1}] \cdot (\hat{\boldsymbol{k}} \sin\theta\sin\phi + \hat{\boldsymbol{\theta}} \cos\theta\sin\phi + \hat{\boldsymbol{\phi}} \cos\phi) \\ &= -\hat{\boldsymbol{\theta}} \cos\theta\sin\phi - \hat{\boldsymbol{\phi}} \cos\phi \quad \text{(C.24)}\end{aligned}$$

$$\hat{\boldsymbol{k}} \times (\hat{\boldsymbol{k}} \times \hat{\boldsymbol{z}}) = [\hat{\boldsymbol{k}}\hat{\boldsymbol{k}} - \mathbf{1}] \cdot (\hat{\boldsymbol{k}} \cos\theta - \hat{\boldsymbol{\theta}} \sin\theta) = \hat{\boldsymbol{\theta}} \sin\theta. \quad \text{(C.25)}$$

Bringing it all together, the far field is then

$$\begin{aligned}
\boldsymbol{F}^{(m)}(\theta,\phi) &= \frac{\mathrm{j}k}{4\pi}\hat{\boldsymbol{k}} \times \iint_S \Big[\boldsymbol{E}^{(m)}(\boldsymbol{r}) \times \hat{\boldsymbol{n}} + \eta_0 \hat{\boldsymbol{k}} \times (\hat{\boldsymbol{n}} \times \boldsymbol{H}^{(m)}(\boldsymbol{r}))\Big] \, \mathrm{e}^{\mathrm{j}(k\hat{\boldsymbol{k}}\cdot\boldsymbol{r} - m\varphi)} \, \mathrm{d}S \\
&= \frac{\mathrm{j}k}{2}\mathrm{j}^m \mathrm{e}^{-\mathrm{j}m\phi} \int_{\boldsymbol{\rho}\in\gamma} \Big(- \big[n_z E_\varphi^{(m)} C_m - (n_\rho E_z^{(m)} - n_z E_\rho^{(m)}) S_m\big] \underbrace{(\hat{\boldsymbol{\phi}}\cos\theta\cos\phi + \hat{\boldsymbol{\theta}}\sin\phi)}_{=\hat{\boldsymbol{k}}\times\hat{\boldsymbol{x}}} \\
&\qquad - \big[n_z E_\varphi^{(m)} S_m + (n_\rho E_z^{(m)} - n_z E_\rho^{(m)}) C_m\big] \underbrace{(\hat{\boldsymbol{\phi}}\cos\theta\sin\phi - \hat{\boldsymbol{\theta}}\cos\phi)}_{=\hat{\boldsymbol{k}}\times\hat{\boldsymbol{y}}} \\
&\qquad - n_\rho E_\varphi^{(m)} A_m \underbrace{(-\hat{\boldsymbol{\phi}}\sin\theta)}_{=\hat{\boldsymbol{k}}\times\hat{\boldsymbol{z}}} \\
&\quad + \eta_0 \big[n_z H_\varphi^{(m)} C_m - (n_\rho H_z^{(m)} - n_z H_\rho^{(m)}) S_m\big] \underbrace{(-\hat{\boldsymbol{\theta}}\cos\theta\cos\phi + \hat{\boldsymbol{\phi}}\sin\phi)}_{=\hat{\boldsymbol{k}}\times(\hat{\boldsymbol{k}}\times\hat{\boldsymbol{x}})} \\
&\quad + \eta_0 \big[n_z H_\varphi^{(m)} S_m + (n_\rho H_z^{(m)} - n_z H_\rho^{(m)}) C_m\big] \underbrace{(-\hat{\boldsymbol{\theta}}\cos\theta\sin\phi - \hat{\boldsymbol{\phi}}\cos\phi)}_{=\hat{\boldsymbol{k}}\times(\hat{\boldsymbol{k}}\times\hat{\boldsymbol{y}})} \\
&\qquad + \eta_0 n_\rho H_\varphi^{(m)} A_m \underbrace{\hat{\boldsymbol{\theta}}\sin\theta}_{=\hat{\boldsymbol{k}}\times(\hat{\boldsymbol{k}}\times\hat{\boldsymbol{z}})} \Big) \mathrm{e}^{\mathrm{j}kz\cos\theta} \rho \, \mathrm{d}\ell. \qquad \text{(C.26)}
\end{aligned}$$

Our final result is then

$$\begin{aligned}
\boldsymbol{F}^{(m)}(\theta,\phi) &= \hat{\boldsymbol{\theta}} \frac{\mathrm{j}k}{2}\mathrm{j}^m \mathrm{e}^{-\mathrm{j}m\phi} \int_{\boldsymbol{\rho}\in\gamma} \Big\{ - \big[C_m n_z E_\varphi^{(m)} - S_m(n_\rho E_z^{(m)} - n_z E_\rho^{(m)})\big] \sin\phi \\
&\qquad + \big[S_m n_z E_\varphi^{(m)} + C_m(n_\rho E_z^{(m)} - n_z E_\rho^{(m)})\big] \cos\phi \\
&\qquad - \eta_0 \big[C_m n_z H_\varphi^{(m)} - S_m(n_\rho H_z^{(m)} - n_z H_\rho^{(m)})\big] \cos\theta\cos\phi \\
&\qquad - \eta_0 \big[S_m n_z H_\varphi^{(m)} + C_m(n_\rho H_z^{(m)} - n_z H_\rho^{(m)})\big] \cos\theta\sin\phi \\
&\qquad + \eta_0 A_m n_\rho H_\varphi^{(m)} \sin\theta \Big\} \mathrm{e}^{\mathrm{j}kz\cos\theta} \rho \, \mathrm{d}\ell \\
&\quad + \hat{\boldsymbol{\phi}} \frac{\mathrm{j}k}{2}\mathrm{j}^m \mathrm{e}^{-\mathrm{j}m\phi} \int_{\boldsymbol{\rho}\in\gamma} \Big\{ - \big[C_m n_z E_\varphi^{(m)} - S_m(n_\rho E_z^{(m)} - n_z E_\rho^{(m)})\big] \cos\theta\cos\phi \\
&\qquad - \big[S_m n_z E_\varphi^{(m)} + C_m(n_\rho E_z^{(m)} - n_z E_\rho^{(m)})\big] \cos\theta\sin\phi \\
&\qquad + A_m n_\rho E_\varphi^{(m)} \sin\theta \\
&\qquad + \eta_0 \big[C_m n_z H_\varphi^{(m)} - S_m(n_\rho H_z^{(m)} - n_z H_\rho^{(m)})\big] \sin\phi \\
&\qquad - \eta_0 \big[S_m n_z H_\varphi^{(m)} + C_m(n_\rho H_z^{(m)} - n_z H_\rho^{(m)})\big] \cos\phi \Big\} \mathrm{e}^{\mathrm{j}kz\cos\theta}, \rho \, \mathrm{d}\ell \qquad \text{(C.27)}
\end{aligned}$$

which gives the far field amplitude for azimuthal mode m at any direction (θ, ϕ).

References

[1] M. Abramowitz and I. A. Stegun, eds. "Handbook of Mathematical Functions". Applied Mathematics Series No. 55. National Bureau of Standards, 1970.

[2] M. S. Alnaes, A. Logg, K. B. Ølgaard, M. E. Rognes, and G. N. Wells. "Unified form language: a domain-specific language for weak formulations of partial differential equations". *ACM Transactions on Mathematical Software* 40 (2014).

[3] I. A. Baratta, J. P. Dean, J. S. Dokken, M. Habera, J. S. Hale, C. N. Richardson, M. E. Rognes, M. W. Scroggs, N. Sime, and G. N. Wells. *DOLFINx: the next generation FEniCS problem solving environment*. preprint. 2023.

[4] C. Geuzaine and J.-F. Remacle. "Gmsh: a 3-D finite element mesh generator with built-in pre-and post-processing facilities". *International journal for numerical methods in engineering* 79 (11) (2009): pp. 1309–1331.

[5] J. E. Hansen, ed. "Spherical Near-Field Antenna Measurements". IEE electromagnetic waves series 26. Peter Peregrinus Ltd., 1988.

[6] D. J. Kozakoff. "Analysis of radome-enclosed antennas". Artech House, 2010.

[7] G. Kristensson. *Verification of radome problems—Part I*. Tech. rep. LUTEDX/(TEAT-7262)/1-30/(2018). Dept Electrical and Information Technology, Lund University, Sweden, 2018.

[8] G. Kristensson. *Verification of radome problems—Part II*. Tech. rep. LUTEDX/(TEAT-7270)/1-26/(2020). Dept Electrical and Information Technology, Lund University, Sweden, 2020.

[9] J. Nitsche. "Über ein variationsprinzip zur lösung von dirichlet-problemen bei verwendung von teilräumen, die keinen randbedingungen unterworfen sind". In: *Abhandlungen aus dem mathematischen Seminar der Universität Hamburg*. Vol. 36. 1. Springer. 1971, pp. 9–15.

[10] S. Poulsen. "Stealth radomes". PhD thesis. Lund University, 2006.

[11] S. Prahl. *miepython: A Python library for Mie scattering calculations*. Version latest. 2025.

[12] M. W. Scroggs, I. A. Baratta, C. N. Richardson, and G. N. Wells. "Basix: a runtime finite element basis evaluation library". *Journal of Open Source Software* 7 (73) (2022): p. 3982.

[13] M. W. Scroggs, J. S. Dokken, C. N. Richardson, and G. N. Wells. "Construction of arbitrary order finite element degree-of-freedom maps on polygonal and polyhedral cell meshes". *ACM Transactions on Mathematical Software* 48 (2) (2022): 18:1–18:23.

[14] R. Shavit. "Radome electromagnetic theory and design". John Wiley & Sons, 2018.

[15] D. Sjöberg. *Computation of radome reference cases using a rotationally symmetric full wave solver*. Tech. rep. LUTEDX/(TEAT-7273)/1–23/(2022). Dept Electrical and Information Technology, Lund University, Sweden, 2022.

[16] D. Sjöberg. "Full wave verification of radome edge scattering treatments using open source tools". In: *European Conference on Antennas and Propagation (EuCAP) 2024*. 2024.

[17] A. Taflove, S. C. Hagness, and M. Piket-May. "The electrical engineering handbook". In: Elsevier, 2004. Chap. Computational Electromagnetics: The Finite-Difference Time-Domain Method, pp. 629–670.

[18] W. J. Wiscombe. "Improved Mie scattering algorithms". *Applied optics* 19 (9) (1980): pp. 1505–1509.